Coupling of three-spin qubits to their electric environment

Maximilian Russ, Florian Ginzel, and Guido Burkard

Department of Physics, University of Konstanz, D-78457 Konstanz, Germany

(Received 8 July 2016; revised manuscript received 16 September 2016; published 13 October 2016)

We investigate the behavior of qubits consisting of three electron spins in double and triple quantum dots subject to external electric fields. Our model includes two independent bias parameters, ε and ε_M, which both couple to external electromagnetic fields and can be controlled by gate voltages applied to the quantum dot structures. By varying these parameters, one can switch the qubit type by shifting the energies in the single quantum dots, thus changing the electron occupancy in each dot. Starting from the asymmetric resonant exchange qubit with a (2,0,1) and (1,0,2) charge admixture, one can smoothly cross over to the resonant exchange qubit with a detuned (1,1,1) charge configuration, and to the exchange-only qubit with the same charge configuration but equal energy levels down to the hybrid qubits with (1,2,0) and (0,2,1) charge configurations. Here, (l,m,n) describes a configuration with l electrons in the left dot, m electrons in the center dot, and n electrons in the right dot. We first focus on random electromagnetic field fluctuations, i.e., "charge noise," at each quantum dot resulting in dephasing of the qubit, and we provide a complete map of the resulting dephasing time as a function of the bias parameters. We pay special attention to the so-called sweet spots and double sweet spots of the system, which are least susceptible to noise. In the second part, we investigate the coupling of the qubit system to the coherent quantized electromagnetic field in a superconducting strip-line cavity, and we also provide a complete map of the coupling strength as a function of the bias parameters. We analyze the asymmetric qubit-cavity coupling via ε and the symmetric coupling via ε_M.

I. INTRODUCTION

Qubits based on the spin of electrons trapped in quantum dots (QDs) [1] are a leading candidate for enabling quantum information processing. They provide long coherence times [2–12], together with a scalable architecture for a dense qubit implementation. Semiconductor materials such as gallium arsenide (GaAs) [13] and silicon [14] are the most common choices as the host material for QDs. One common feature of these implementations is the need for control with electric fields at the nanoscale, which unavoidably couples the qubit system to electrical noise [1]. Dominating sources of decoherence are nuclear spins [15–17], spin-orbit interaction [18,19], and charge noise from either the environment or the confining gates [20–25]. The effect of the first and second source of decoherence can be drastically reduced by using silicon as the host material due to its highly abundant nuclear spin free isotope and a weak spin-orbit interaction [21]. Using active noise suppression methods such as quantum error correction [26] and composite pulse sequences [27–29] leaves charge noise coupled to the spin as the remaining problem to be taken care of. Thus, additional passive suppression methods are needed, such as optimal working points (sweet spots) [30,31], which vary in effectiveness for different qubit implementations.

Qubit implementations using single or multiple QDs to encode a single qubit show high-fidelity gate operations, long decoherence times, together with fast qubit control, allowing for many operations during the qubit lifetime [6,32–35]. An advantage of multispin qubit encodings consists in their improved protection against certain types of noise [36] together with faster gate operations [37–41]. This ultimately leads to the three-spin-$\frac{1}{2}$ qubits (see Fig. 1); the exchange-only (EO) qubit allowing for full qubit control with only the exchange

interaction [37], the resonant exchange (RX) qubit with permanently acting exchange interaction and control through resonant driving [22,24,34], and the always-on exchange-only (AEON) qubit with symmetric gate control [25]. Robustness against charge noise can be achieved by operating the qubit on sweet spots [22] where the qubit energy splitting is extremal with respect to one noisy parameter, or double sweet spots [25,42] where both noisy parameters are optimized. In this paper, we provide a full analysis of charge noise for three-spin-$\frac{1}{2}$ qubits (Fig. 1), and we present optimal working points. We go beyond previous work [24,25] by exploring the full $(\varepsilon,\varepsilon_M)$ parameter space. Moreover, we include two noisy tunneling parameters mapping the resulting dephasing time in this parameter space. Single sweet spots (SSSs) and double sweet spots (DSSs) are presented for both types of
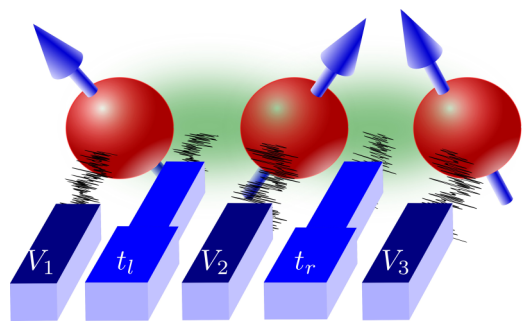

FIG. 1. Schematic illustration of a three-spin qubit coupled to a noisy electric environment. The environment can affect the electron spins directly through the gate voltages V_i with $i \in \{1,2,3\}$ of each quantum dot (QD) or the exchange coupling (green cloud) between the electron spins through the gate-controlled tunnel hopping (t_l and t_r).

noisy parameters and combined to provide the best working points.

In this paper, we neglect relaxation and dephasing effects from electric noise originating from phonons coupled to the dipole moment of the qubit [13,16,22] due to their much longer time scales. The time scales for spin relaxation are on the order of milliseconds ($B \approx 4\,T$) to seconds ($B \approx 1\,T$) in GaAs [16,22,43] and several orders of magnitude longer in silicon due to the lack of piezoelectric phonons in unstrained silicon [14,44].

Two-qubit gates are provided by the exchange interaction [25,28,37,45–47], Coulomb interaction [22,48,49], and cavity-mediated coupling [42,44], while the range of the latter is only limited by the extension of the cavity. This long-ranged coupling technique can be realized within the approach of cavity electrodynamics (cQED) by coupling the qubit capacitively to a superconducting strip-line cavity [50,51] adapted for spin qubits [42,44,52–62]. Implementing a three-spin qubit in a triple quantum dot (TQD) coupled to a cavity is possible for two distinct setups: a longitudinal coupling or asymmetric setup and a transversal or symmetric coupling [42]. In this paper, both of these setups are discussed, going beyond previous work for the asymmetric implementation [42] and providing a microscopic description for both implementations.

This paper is organized as follows. In Sec. II, we define the three-spin qubit states, and we discuss the different regimes in parameter space where each qubit implementation is located and their conversion into each other. In Sec. III, we analyze in detail the optimal working points best suitable for operating the qubit in the presence of charge noise coupled to the qubit through detuning and tunnel parameters. Subsequently in Sec. IV, we present two setups for coupling three-spin qubits to a superconducting strip-line cavity in order to find operation points with a strong and controllable coupling. We conclude in Sec. V with a summary and outlook.

II. QUBIT

We consider the spins of three electrons in a linearly arranged triple quantum dot (TQD) (Fig. 1) where each QD has a single available orbital, whereas higher orbitals are energetically unfavorable due to a strong confinement. Additionally, we restrict ourselves to the spin degree of freedom (DOF) only, hence we either consider a material with no valley DOF or a strong valley splitting surpassing the energy of the exchange splittings and then treat the valley as an orbital DOF. Further, we assume that the TQD is connected to an electric environment (schematically illustrated in Fig. 1) via the gate voltages V_i of QD i with $i \in \{1,2,3\}$ and via the gate-controlled tunnel barriers, which, in addition to a static classical part, consist of random electric fluctuations and a coherent quantized electric field. As a model of the TQD, we use the three-site extended Hubbard model

$$
H_{\text{Hub}} = \sum_{i=1}^{3} \left[\frac{\tilde{U}}{2} n_i (n_i - 1) + V_i n_i \right]
$$
$$
+ \sum_{\langle i,j \rangle} \left[U_C n_i n_j + \sum_{\sigma=\uparrow,\downarrow} (t_{ij} c_{i,\sigma}^\dagger c_{j,\sigma} + \text{H.c.}) \right], \quad (1)
$$

where $c_{i,\sigma}^\dagger$ ($c_{i,\sigma}$) creates (annihilates) an electron in QD i with spin σ. We define the number operator $n_i = \sum_\sigma c_{i,\sigma}^\dagger c_{i,\sigma}$ and the gate-controlled pairwise hopping matrix elements t_{ij} with $i,j \in \{1,2,3\}$. Here, we consider symmetric, spin-conserving nearest-neighbor hopping, $t_{13} = t_{31} = 0$, $t_{12} = t_{21} \equiv t_l/\sqrt{2}$, and $t_{23} = t_{32} \equiv t_r/\sqrt{2}$. We also include the Coulomb repulsion of two electrons in the same QD $\tilde{U}$ and in neighboring QDs U_C, which leads to a static energy shift in the dots.

Restricting ourselves to the subspace of the three-spin Hilbert space with total spin $S = S_z = 1/2$, we identify six relevant states, two states with a (1,1,1) charge configuration, and one each with a (2,0,1), (1,0,2), (1,2,0), and (0,2,1) charge configuration,

$$
|0\rangle \equiv \frac{1}{\sqrt{2}} (c_{1,\uparrow}^\dagger c_{2,\uparrow}^\dagger c_{3,\downarrow}^\dagger - c_{1,\downarrow}^\dagger c_{2,\uparrow}^\dagger c_{3,\uparrow}^\dagger) |\text{vac}\rangle
$$
$$
= |s\rangle_{13} |\uparrow\rangle_2, \quad (2)
$$

$$
|1\rangle \equiv \frac{1}{\sqrt{6}} (2 c_{1,\uparrow}^\dagger c_{2,\downarrow}^\dagger c_{3,\uparrow}^\dagger - c_{1,\uparrow}^\dagger c_{2,\uparrow}^\dagger c_{3,\downarrow}^\dagger - c_{1,\downarrow}^\dagger c_{2,\uparrow}^\dagger c_{3,\uparrow}^\dagger) |\text{vac}\rangle
$$
$$
= \sqrt{\frac{2}{3}} |t_+\rangle_{13} |\downarrow\rangle_2 - \frac{1}{\sqrt{3}} |t_0\rangle_{13} |\uparrow\rangle_2, \quad (3)
$$

$$
|2\rangle \equiv c_{1,\uparrow}^\dagger c_{1,\downarrow}^\dagger c_{3,\uparrow}^\dagger |\text{vac}\rangle = |s\rangle_{11} |\uparrow\rangle_3, \quad (4)
$$

$$
|3\rangle \equiv c_{1,\uparrow}^\dagger c_{3,\uparrow}^\dagger c_{3,\downarrow}^\dagger |\text{vac}\rangle = |\uparrow\rangle_1 |s\rangle_{33}, \quad (5)
$$

$$
|4\rangle \equiv c_{1,\uparrow}^\dagger c_{2,\uparrow}^\dagger c_{2,\downarrow}^\dagger |\text{vac}\rangle = |\uparrow\rangle_1 |s\rangle_{22}, \quad (6)
$$

$$
|5\rangle \equiv c_{2,\uparrow}^\dagger c_{2,\downarrow}^\dagger c_{3,\uparrow}^\dagger |\text{vac}\rangle = |s\rangle_{22} |\uparrow\rangle_3, \quad (7)
$$

where $|\text{vac}\rangle$ denotes the vacuum state, $|s\rangle_{ij}$ denotes the singlet state, $|t_0\rangle_{ij}$ denotes the $S_z = 0$ triplet state, and $|t_+\rangle_{ij}$ denotes the $S_z = +1$ triplet state. Here, (l,m,n) describes a configuration with l electrons in the left dot, m electrons in the center dot, and n electrons in the right dot. An additional leakage state with $S = 3/2$ and $S_z = 1/2$ is not coupled since charge noise conserves the total spin S.

We introduce a new set of detuning parameters $V_{\text{tot}} = (V_1 + V_2 + V_3)/3$, $\varepsilon \equiv (V_1 - V_3)/2$, and $\varepsilon_M \equiv V_2 - (V_1 + V_3)/2 + U_C$. The parameter V_{tot} merely shifts the total energy, hence it contributes to neither the dynamics of the qubit nor the decoherence. The asymmetric detuning ε is the energy difference between the left QD and the right QD, and the

symmetric detuning ε_M is the energy difference between the center QD and the mean of the outer QDs. Defining the charging energy $U \equiv \tilde{U} - U_C$, we find for the Hamiltonian Eq. (1) in the $S = S_z = 1/2$ basis $\{|0\rangle, |1\rangle, |2\rangle, |3\rangle, |4\rangle, |5\rangle\}$ the matrix representation

$$
H = \begin{pmatrix}
0 & 0 & \frac{1}{2}t_l & \frac{1}{2}t_r & \frac{1}{2}t_r & \frac{1}{2}t_l \\
0 & 0 & \frac{\sqrt{3}}{2}t_l & -\frac{\sqrt{3}}{2}t_r & -\frac{\sqrt{3}}{2}t_r & \frac{\sqrt{3}}{2}t_l \\
\frac{1}{2}t_l & \frac{\sqrt{3}}{2}t_l & \varepsilon - \varepsilon_M + U & 0 & 0 & 0 \\
\frac{1}{2}t_r & -\frac{\sqrt{3}}{2}t_r & 0 & -\varepsilon - \varepsilon_M + U & 0 & 0 \\
\frac{1}{2}t_r & -\frac{\sqrt{3}}{2}t_r & 0 & 0 & \varepsilon + \varepsilon_M + U & 0 \\
\frac{1}{2}t_l & \frac{\sqrt{3}}{2}t_l & 0 & 0 & 0 & -\varepsilon + \varepsilon_M + U
\end{pmatrix}. \tag{8}
$$

We assume $t_{l,r}$ to be real since any complex phase only contributes a global phase to the eigenstates.

Depending on the position in the $(\varepsilon, \varepsilon_M)$ plane, different qubit implementations are realized (Fig. 2). Directly in the center of the (1,1,1) charge occupancy region, the *exchange-only (EO) qubit* [37] and the *always-on exchange-only (AEON) qubit* [25] are located. Still in the (1,1,1) charge occupancy, but in the area with $\varepsilon_M \gg \varepsilon$, which allows transitions into the (2,0,1) and (1,0,2) charge states, we find the *resonant exchange (RX) qubit* (white dashed triangle). The *asymmetric resonant exchange (ARX) qubit* is located deeper into the regime with $\varepsilon_M \gg \varepsilon$ and a strong mixture of (2,0,1) and (1,0,2) charge configurations [24]. Due to mirror symmetry, four DSSs can be found (black dots) in the corner of the diamond-shaped

FIG. 2. Energy landscape of the ground-state energy gap ω as a function of the detuning parameters ε and ε_M in units of the charging energy U. For the tunneling parameters, we used $t_l = 0.022\,U$ and $t_r = 0.015\,U$. Maneuvering through the $(\varepsilon, \varepsilon_M)$ plane, one can access various parameter regimes that allow the use of different qubit implementations in different charge configurations (l,m,n), where l electrons are in the left, m electrons in the center, and n electrons in the right QD. We further highlight the double sweet spots (DSSs) (black dots), the location of the exchange-only (EO) qubit, the resonant exchange (RX) qubit (dashed triangle), the asymmetric resonant exchange (ARX) qubit, and the left and right hybrid ($H_{l,r}$) qubit.

(1,1,1) charge configuration area. At the bottom left (right) in the $(\varepsilon, \varepsilon_M)$ plane in Fig. 2, only two neighboring QDs are occupied by three electrons giving rise to the double quantum dot (DQD) *hybrid qubit* [39–41] formed in QD 1 and QD 2 (QD 2 and QD 3).

III. CHARGE DEPHASING

Recent progress for spin qubits using purified silicon as the host material has lead to exceptionally long T_1 and T_2 times, emphasizing the importance of charge noise. The use of isotopically purified Si eliminates nuclear spins as the leading source for decoherence and leaves charge noise as the main cause of decoherence [21]. Therefore, while our analysis is general and valid for all material systems, it is particularly relevant for spin qubits in Si. Charge noise or electrical noise originates from random charge fluctuations of the material or from the control and confinement voltages giving rise to fluctuating energies. Formally, we describe this by substituting $q \to q + \delta q$, in which the parameter $q \in \{\varepsilon, \varepsilon_M, t_l, t_r\}$ is affected by random fluctuations $\delta q \in \{\delta\varepsilon, \delta\varepsilon_M, \delta t_l, \delta t_r\}$. There are two effects of decoherence for charge noise, namely longitudinal and transversal dephasing, where the first causes the energy gap between the qubit states $|e\rangle$ and $|g\rangle$ to fluctuate while the second gives rise to transitions between the qubit states. These can be divided further into decoherence due to detuning parameters [22–25] $(\varepsilon, \varepsilon_M)$ and decoherence due to charge noise coupled to the qubit by tunneling (t_l, t_r).

The remainder of this section is organized as follows. First, we present a generalized framework extending previous models describing charge noise coupled to the qubit to different control parameters. In the next step, we take only individual control parameters into account. We start with longitudinal and transversal noise originating from the detuning parameters ε and ε_M, and we identify sweet spots [22–25], i.e., working points in which the qubits lifetime is highly increased due to vanishing coupling in first order of the qubit to the noise. Subsequently, we focus on the effects of noise coupled to the qubit via fluctuations of the tunnel amplitude, and we show that there exist no sweet spots for both noisy tunneling parameters simultaneously. In the last part of this section, we take all separately discussed effects of the noisy parameters into account in order to present the best working points.
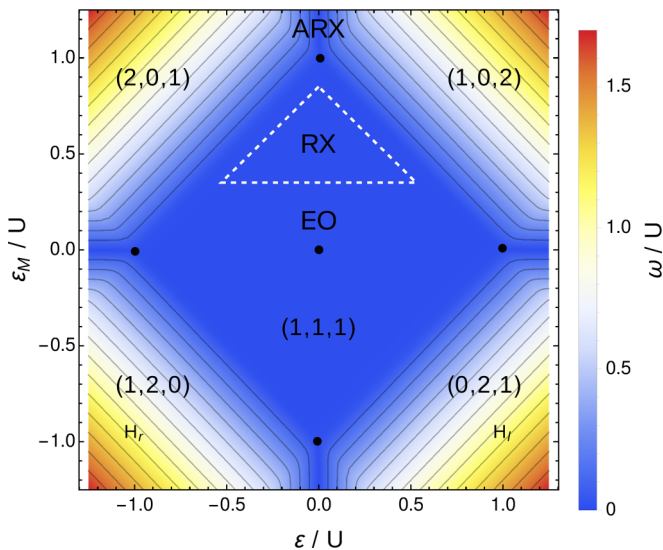
A. General framework

In general, we can write the qubit Hamiltonian in its eigenbasis [24], $\{|g\rangle, |e\rangle\}$, as

$$H_{\text{noise}} = \frac{\hbar}{2}[(\omega + \delta\omega_z)\sigma_z + \delta\omega_x\sigma_x + \delta\omega_y\sigma_y], \quad (9)$$

with the unperturbed energy gap $\hbar\omega$ between the qubit states. Here, $|e\rangle$ and $|g\rangle$ are the two lowest eigenstates of H in Eq. (8). The longitudinal effect of the charge noise up to second order is

$$\delta\omega_z = \sum_q \left(\omega_q \delta q + \frac{\omega_{q,q}}{2}\delta q^2 \right) + \frac{1}{2}\sum_{p \neq q} \omega_{p,q}\delta p\,\delta q, \quad (10)$$

where we used the definitions $\omega_q \equiv \frac{\partial\omega}{\partial q}$ and $\omega_{p,q} \equiv \frac{\partial^2\omega}{\partial p\partial q}$ with $p,q \in \{\varepsilon, \varepsilon_M, t_l, t_r\}$. For the transversal effects, we consider

$$\delta\omega_x = \sum_q \delta\omega_{x,q}\delta q, \quad (11)$$

with $\delta\omega_{x,q} \equiv \langle g| H_{1,q} |e\rangle$ and $\delta\omega_y = 0$ due to real valued tunneling. Here, $H_{1,q}$ is the part of the Hamiltonian from Eq. (8) associated with the perturbation in q, thus $H_{1,q} = \frac{\partial}{\partial q}H\,\delta q$. Considering only longitudinal noise, one can calculate the pure dephasing in a Ramsey free decay approach [55],

$$\tilde{f}(t) \equiv \langle e^{i\phi(t)} \rangle = e^{-\langle\phi(t)^2\rangle} = e^{-t^2/T_\varphi^2} \quad (12)$$

with $\phi(t) \equiv \int_{t_0}^t dt'\delta\omega_z(t')$ in which we used $\delta q = \delta q(t)$. For the first equality we used Gaussian-distributed noise with zero mean, while for the second equality we used a spectral density exponent [63] $\gamma = 1$. This allows us to calculate for a given spectral density of the noise $S_q(\tilde{\omega}) = A_q|\tilde{\omega}|^{-\gamma}$ the associated dephasing time [24],

$$T_\varphi = \hbar \left[\sum_q \frac{\omega_q^2}{2} A_p \log r + \frac{\omega_{q,q}^2}{4} A_q^2 \log^2 r \right.$$

$$\left. + \frac{1}{2}\sum_{p\neq q} \frac{\omega_{p,q}^2}{2} A_p A_q \log^2 r + \frac{1}{8}\omega_{p,p}\omega_{q,q}A_p A_q \right]^{-\frac{1}{2}}. \quad (13)$$

Here, we assumed independent and uncorrelated noise for each noisy parameter $p,q \in \{\varepsilon, \varepsilon_M, t_l, t_r\}$, and we used the ratio $r \equiv \omega_{\text{UV}}/\omega_{\text{IR}}$ of the lower frequency cutoff ω_{IR} and the upper frequency cutoff ω_{UV} needed to ensure convergence of the integral.

With this in mind, we formally define the expression "sweet spot" initially introduced as the best points for operations due to a vanishing coupling of the qubit to the noise in first order. Assuming first-order noise effects to be the dominant ones, these points yield the longest lifetime of the qubit according to Eq. (13), and therefore the ideal operation points for the qubit. Taking only first-order effects into account, we obtain for the best working points the condition

$$\sum_q \omega_q \delta q = 0, \quad (14)$$

which is in general only possible for each $\omega_q = 0$ with $q \in \{\varepsilon, \varepsilon_M, t_l, t_r\}$. We now define a single "sweet spot" (SSS) if

this condition is fulfilled for one noisy parameter. Analogously, we define a "double sweet spot" (DSS) if $\omega_q = \omega_p = 0$ with $q \neq p \in \{\varepsilon, \varepsilon_M, t_l, t_r\}$. Considering a total of four noisy parameters, we can also introduce "triple" and "quadruple sweet spots" in which Eq. (14) is for three noisy parameters or completely fulfilled. Unfortunately, we find that there exist no nontrivial quadruple sweet spots in a three-spin-$\frac{1}{2}$ qubit in maximally three QDs. A trivial quadruple sweet spot $\varepsilon = \varepsilon_M = t_l = t_r = 0$ cannot be used for quantum computing since no gates can be performed, but instead it can be useful for quantum storage. However, turning off the exchange interaction increases decoherence effects due to magnetic noise [17].

The second term in the Hamiltonian [see Eq. (9)] $\delta\omega_x$ leads to random rotations of the qubit around the x axis with time scales on the order of ms for realistic charge noise (assuming $\sqrt{\langle\delta q^2\rangle} = 1\,\mu\text{eV}$ at 1 Hz) [63]. Somewhat more devastating for the qubit is the fact that transversal charge noise changes the orientation of the eigenstates and therefore the energy gap giving rise to an additional term for the dephasing in second order of the fluctuations. This becomes clear when expanding the eigenenergy difference from Eq. (9),

$$\omega = \sqrt{(\omega_0 + \delta\omega_z)^2 + \delta\omega_x^2 + \delta\omega_y^2}$$

$$\simeq \omega_0 + \delta\omega_z + \frac{\delta\omega_x^2}{2\omega_0} + \frac{\delta\omega_y^2}{2\omega_0} + O(\delta\omega^3). \quad (15)$$

Inside the (1,1,1) charge configuration regime and away from the charge transition lines, the states $|0\rangle$ and $|1\rangle$ defined in Eqs. (3) and (4) are nearly the qubit states, while the coupling of the other states can be taken into account using a low-energy Schrieffer-Wolff approximation [64]. We obtain for the resonance frequency between the qubit eigenstates [25]

$$\hbar\omega = \sqrt{J^2 + 3j^2}, \quad (16)$$

with the mean $J \equiv (J_l + J_r)/2$ and half of the difference $j \equiv (J_l - J_r)/2$ of the left and right exchange interaction and between the left (right) QD and the center QD, respectively,

$$J_l = 2t_l^2 U/[U^2 - (\varepsilon - \varepsilon_M)^2], \quad (17)$$

$$J_r = 2t_r^2 U/[U^2 - (\varepsilon + \varepsilon_M)^2]. \quad (18)$$

Utilizing this, we find a closed analytical expression for the longitudinal fluctuation,

$$\omega_q = (J\partial_q J + 3j\partial_q j)/\omega, \quad (19)$$

and the transversal effect,

$$\delta\omega_{x,q} = (J\partial_q j - j\partial_q J)/\omega, \quad (20)$$

in the (1,1,1) charge regime. For $\varepsilon_M \gg 0$ (RX regime), these results converge with the expressions considering only the RX qubit [24], since there the influence of the states $|4\rangle$ and $|5\rangle$ becomes negligible.

B. Detuning noise

Longitudinal dephasing T_φ due to low-frequency charge noise originating from the detuning parameters ε and ε_M is usually seen as the dominant source for decoherence. For reasons of simplicity, we set in this subsection $\delta t_l = \delta t_r = 0$,

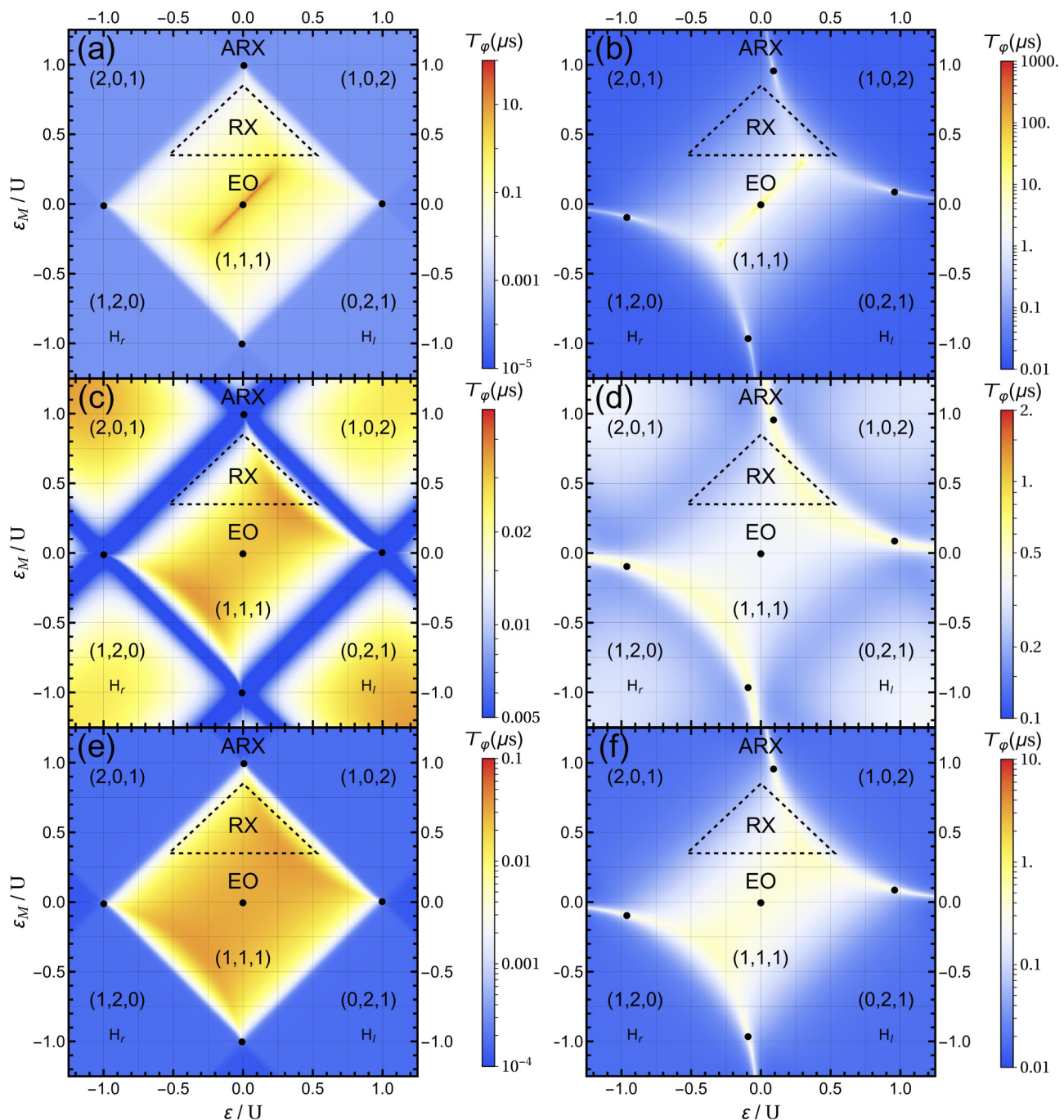FIG. 3. Dephasing time T_φ given by Eq. (13) due to longitudinal noise as a function of the detuning parameters ε and ε_M. In the top row [(a) and (b)] we plot T_φ resulting from charge noise in the two detuning parameters ε and ε_M, in the center row [(c) and (d)] we plot T_φ resulting from charge noise in the two tunneling parameters t_l and t_r, and in the bottom row [(e) and (f)] we plot T_φ resulting from charge noise from all four parameters combined, where we choose the parameter settings identical in each column. The left column shows results for weak tunneling and strong noise, while in the right column, results for strong tunneling and weak noise are plotted. Parameters are set as follows: $t_l = 0.022\,U$, $t_r = 0.015\,U$, $A_q = (10^{-3}\,U)^2$, where $q = \varepsilon, \varepsilon_M$ in (a) and (e), and $A_q = (10^{-4}\,U)^2$, where $q = t_l, t_r$ in (c) and (e), for the left column, and $t_l = 0.22\,U$, $t_r = 0.15\,U$, $A_q = (10^{-5}\,U)^2$, where $q = \varepsilon, \varepsilon_M$ in (b) and (f), and $A_{t_l} = A_{t_r} = (10^{-6}\,U)^2$, where $q = t_l, t_r$ in (d) and (f), for the right column. To include a large frequency bandwidth, we globally set the ratio of the lower and higher frequency cutoff $r = 5 \times 10^6$. For the scale of T_φ, we used an explicit value of $U = 1\,\mathrm{meV}$; note that T_φ scales inversely proportional with U. The black dots indicate the DSSs.

and we only consider charge noise originating from the detuning parameters $\delta\varepsilon \neq 0$ and $\delta\varepsilon_M \neq 0$. The effect of this can be drastically reduced by working on SSS [22] or DSS [23–25]. They fulfill the condition $\omega_\varepsilon = \omega_{\varepsilon_M} = 0$ such that

the longitudinal coupling given in Eq. (10) vanishes and only second-order effects remain.

In Figs. 3(a) and 3(b), we plot the resulting dephasing time T_φ given in Eq. (13) as a function of the detuning

parameters considering only longitudinal noise originating from ε and ε_M for different parameter settings. We find in total five DSSs for the three-spin qubit marked as black dots. Two DSSs are already known, one inside the (1,1,1) charge configuration regime [25] and one at the transition between the (2,0,1) and (1,0,2) charge states [24], while the other three DSSs appear at the remaining three charge transitions, located on the left between (2,0,1) and (1,2,0), on the right right between (1,0,2) and (0,2,1), and on the bottom between (1,2,0) and (0,2,1) in the figures due to symmetry considerations. For symmetric tunneling ($t_l = t_r = t$), the five DSSs are approximately located at $(\varepsilon, \varepsilon_M) = (0, U)$, $(0, -U)$, $(-U, 0)$, $(U, 0)$, and $(0, 0)$, while for asymmetric tunneling ($t_l \neq t_r$) all DSSs except the center one are slightly shifted due to a shift of the charge transitions. Comparing these DSSs with each other, the four DSSs located at the charge transitions are unfavorable for a small tunneling and strong noise due to strong higher-order effects limiting the coherence of the qubit. Considering stronger tunneling between the QDs and weaker noise, the higher-order effects are greatly reduced due to softening of the charge transitions. If for some reason working on the DSSs is unpractical, e.g., coupling the qubit to a cavity, one should favor in the case $t_l \neq t_r$ the working points given by $\varepsilon = \varepsilon_M$ [diagonal orange line seen in Fig. 3(a); see also Appendix C].

Comparing the resulting dephasing times considering noise coupled to the qubit through only one of the detuning parameters ε or ε_M [plotted in Figs. 7(a) and 7(e)], we find that the results are mirror-symmetric to each other, with the symmetry axis given by $\varepsilon = \varepsilon_M$. Single sweet spots are found on a straight vertical (horizontal) line passing through the center, and a serpentine vertical (horizontal) line for $t_l \neq t_r$ (a comparison of symmetric and asymmetric tunnel coupling can be found in Appendix C).

Considering transversal noise, we cannot easily find an analytical expression for T_φ using the free decay model from Eq. (12). Thus, we have calculated $\delta\omega_x = |\delta\omega_{x,\varepsilon}| + |\delta\omega_{x,\varepsilon_M}|$ for $\delta\varepsilon = \delta\varepsilon_M \neq 0$ and $\delta t_l = \delta t_r = 0$, which is a good measure for the coupling of noise to the qubit. In Figs. 8(a) and 8(b), we plot the resulting $\delta\omega_x$ for different parameter settings. Note that in these figures, $\delta\omega_x$ rather than the dephasing time is plotted, thus small values lead to a longer lifetime of the qubit. Since transversal noise leads to transitions between the qubit states, this is also a first indication for the strength of the coupling between a qubit and a microwave cavity. Comparison of the results obtained for transversal charge noise (Fig. 8 in Appendix B) and qubit-cavity coupling strength (Fig. 5) shows a high level of agreement, as expected.

Inside the (1,1,1) charge configuration regime, and considering only noisy detuning parameters ε and ε_M, the sweet spot condition from Eq. (14) simplifies to

$$J \partial_\varepsilon J + 3j \partial_\varepsilon j = J \partial_{\varepsilon_M} J + 3j \partial_{\varepsilon_M} j = 0 \qquad (21)$$

with $\partial_{\varepsilon,\varepsilon_M} J = \pm J_l^2(\varepsilon - \varepsilon_M)/2t_l^2 U + J_r^2(\varepsilon + \varepsilon_M)/2t_r^2 U$ and $\partial_{\varepsilon,\varepsilon_M} j = \pm J_l^2(\varepsilon - \varepsilon_M)/2t_l^2 U - J_r^2(\varepsilon - \varepsilon_M)/2t_r^2 U$. There exists only a single complete solution (DSS) in this regime for $\varepsilon = \varepsilon_M = 0$ [25]. In contrast to the other four DSSs, the position of the center DSS is unaffected by the strength of the tunneling couplings t_l and t_r, thus it is more convenient for

symmetric gate operations to use the tunnel couplings as qubit control parameters.

C. Tunnel noise

Symmetric qubit control by tuning the tunneling coupling between the QDs for qubit control has been proposed from the very beginning [65], and recent experiments in Si/SiGe [12] and GaAs [66] indicate that symmetric operations lead to longer coherence times. Working at the symmetric operation points reduces the coupling to the charge noise originating from the detuning parameters, here ε and ε_M, hence operating on a sweet spot relative to these parameters. However, this opens another channel for noise coupling to the qubit systems via fluctuations in the tunnel amplitude, since the tunneling is now gate-controlled and time-dependent. As a result, strong narrow-band filtering cannot be applied as effectively as for the static case. Thus, the tunneling of the electrons is susceptible to charge noise.

In analogy with detuning noise, considering longitudinal noise through the tunnel parameters t_l and t_r can also be drastically reduced by working on sweet spots. Setting the noisy tunnel parameters $\delta t_l \neq 0$ and $\delta t_r \neq 0$ and ignoring noise coupled to the qubit through the detuning parameters $\delta\varepsilon = \delta\varepsilon_M = 0$, we again find preferable working points and single sweet spots associated with either t_l or t_r. The resulting dephasing is plotted in Figs. 3(c) and 3(d) for the same parameter settings used previously. We find the best working points deep inside the (1,1,1) charge-configuration regime, however, unlike in the case of detuning noise, there is no trace of DSSs in the entire observed regime. The best working point we find is located at the center DSS ($\varepsilon = \varepsilon_M = 0$), which is marginally better than the surrounding area, while the other DSSs at the charge transitions appear very unfavorable at first sight. A zoom-in, however, reveals a steep valley with a long dephasing time that is broadened by larger tunneling couplings. Therefore, the lifetime of the qubit at the DSS located at the charge transitions is limited by higher-order effects. Strong tunnel coupling [see Fig. 3(d)] drastically increases the lifetime at these points due to softening of the charge transitions challenging the center DSS.

For the case $\delta t_r = 0$ [see Figs. 7(e) and 7(f) in Appendix A] we find single sweet spots near the charge transition associated with t_r, thus (1,1,1) $\leftrightarrow$ (1,0,2) and (1,1,1) $\leftrightarrow$ (1,2,0) since at these lines in parameter space, hopping from the left QD to the center QD is energetically highly unfavorable. The opposite case $\delta t_l = 0$ is shown in Figs. 7(g) and 7(h) in Appendix A.

Inside the (1,1,1) charge configuration regime, taking only noisy tunneling into account, the sweet spot condition can be simplified to

$$J_l(2J_l - J_r) = J_r(2J_r - J_l) = 0. \qquad (22)$$

This condition is only fulfilled in the trivial case $J_l = J_r = 0$, thus there exist no DSSs for tunneling noise. A single sweet spot corresponding to the tunneling parameter t_l (t_r) requires $J_{r,(l)} = 2J_{l,(r)}$, which simplifies for $\varepsilon = 0$ to $t_{r,(l)} = \pm\sqrt{2}t_{l,(r)}$. However, the best working points are given for an overall symmetric configuration including both tunneling and detuning. Since the DSSs are all located at high symmetry points, the optimal working points are given by $t_l = t_r$. Preferring

points of operation near the states $|3\rangle$ and $|4\rangle$ ($|2\rangle$ and $|5\rangle$), the optimal ratio is $t_l/t_r > 1$ ($t_l/t_r < 1$). However, the benefit is not very large compared to operating on a DSS.

D. Combination

Combining all effects, we plot in Figs. 3(e)–3(f) the dephasing time T_φ, taking into account all four noisy parameters $\varepsilon, \varepsilon_M, t_l, t_r$. Note that we give less weight to the tunneling parameters due to their smaller strength compared to the detuning parameters. As a result, we find that the previous areas with long coherence times considering only detuning noise of the sweet spots become less pronounced and softened due to the absence of DSSs for tunneling. The center DSS still remains as the optimal point of operation in terms of pure coherence time, however it is only slightly better than the surrounding area in the parameter space.

IV. CAVITY QUANTUM ELECTRODYNAMICS (C-QED)

While the coupling to the uncontrolled fluctuations of the electric field at a three-spin qubit leads to dephasing, controlled coupling to a quantized electromagnetic field in a microwave cavity can be used to couple qubits over long distances. However, strong coupling usually comes with strong dephasing, since a large dipole moment can couple both charge noise and a cavity field to the qubit, thus usually a tradeoff has to be taken into account. Going more into detail, one finds a small difference between the couplings: charge noise couples dominantly longitudinally to the qubit, which gives rise to fluctuations in the energy gap, while in our case the cavity field couples mainly transversal to the qubit since one is operating in a rotating frame [42], which enables transitions between the qubit states. Comparing the effect of longitudinal noise with transversal noise, one can see some crucial differences allowing for working points that have weak dephasing as well as strong qubit-cavity coupling. This asymmetry between dephasing and coupling strength can be expressed in terms of the quality factor of the cavity needed to reach strong coupling between two separated qubits.

This section is organized as follows. First we introduce the basic framework for the qubit-cavity coupling. Subsequently, we calculate the qubit-cavity coupling strength for the asymmetric and symmetric architecture in a simple dipole model. In the last part of this section, we compare the results and provide the quality factor needed to achieve strong coupling for both architectures.

A. General framework

We consider three-spin qubits realized in a linear TQD embedded in a superconducting transmission line resonator with a single-photon mode near the resonance frequency of the qubit. Analogous to Sec. III, we calculate the qubit-cavity coupling for the full ($\varepsilon, \varepsilon_M$) plane including all charge configuration numerically, and subsequently we approximate the center of the (1,1,1) charge configuration analytically in order to analyze the results. To generalize our previous analysis [42] to the full range of charge states studied in the previous sections, we extend the existing formalism to include all six relevant states given by Eqs. (3)–(7). We model
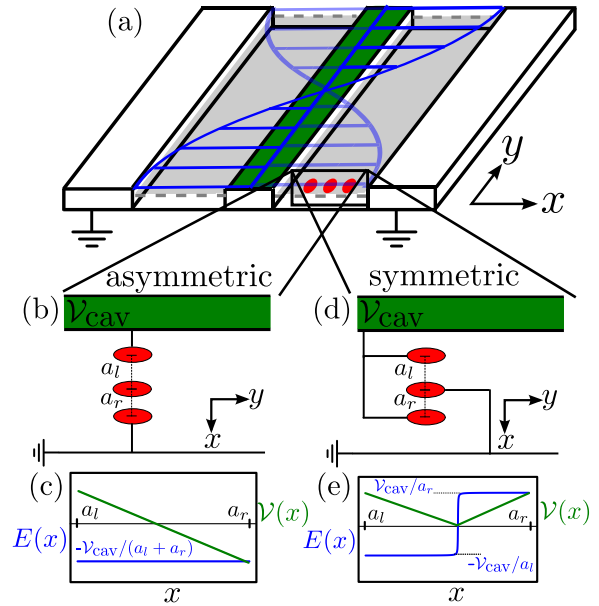

FIG. 4. (a) Schematic illustration of a qubit implemented in a TQD coupled to the cavity and the architecture for a (b) asymmetric and (d) symmetric qubit-cavity coupling. The center conductor of the superconducting transmission line resonator is on the potential $\mathcal{V}_{\mathrm{cav}}$ while the outer conductors are connected to the ground to screen off surrounding fields. The corresponding potential (green) and electric field (blue) are shown for the asymmetric (c) and symmetric (e) arrangement as a function of the position x.

the dipolar interaction [67] between the qubit and the cavity with

$$H_{\mathrm{QC}} = -e\boldsymbol{E}\cdot\hat{\boldsymbol{x}} = -e\boldsymbol{\mathcal{E}}\cdot\hat{\boldsymbol{x}}\,(a + a^\dagger), \qquad (23)$$

and we define the qubit-cavity coupling strength as

$$g \equiv -e\,\langle 0|\,\boldsymbol{\mathcal{E}}\cdot\hat{\boldsymbol{x}}\,|1\rangle, \qquad (24)$$

where $a^\dagger$ (a) creates (annihilates) a photon with frequency ω_{ph} of the cavity mode. Note that in this paper, the formalism using $\boldsymbol{E}\cdot\hat{\boldsymbol{x}}$ is more convenient than the equivalent formalism [67] $\boldsymbol{A}\cdot\hat{\boldsymbol{p}}$ used in previous works [42,54]. Here, $\boldsymbol{E}$ is the quantized electric field, $\boldsymbol{E} = \boldsymbol{\mathcal{E}}(a + a^\dagger)$, and $\boldsymbol{A}$ is the quantized electromagnetic vector potential.

In Fig. 4(a), the basic implementation is shown schematically together with the two architectures discussed in this work, which we label asymmetric and symmetric coupling corresponding to the affected detuning parameter. In this setting, the qubit is placed in the antinode of the electromagnetic field of the cavity to achieve the strongest coupling. The vacuum coupling strength of the interaction is g_0, defined here as the coupling strength of the qubit if $\langle 0|\,\hat{x}\,|1\rangle \cong a_l + a_r$, where $a_{l(r)}$ is the distance between the left (right) QD and the center QD [sketched in Figs. 4(b) and 4(d)]. We find

$$g_0 = -e\mathcal{E}(a_l + a_r) \qquad (25)$$

with $\mathcal{E} = |\boldsymbol{\mathcal{E}}| = \sqrt{\hbar\omega_{\mathrm{ph}}/2\epsilon_0\epsilon v}$, where e is the electron charge, ϵ_0 (ϵ) is the (relative) dielectric constant of the vacuum (material), and v is the volume of the cavity [67]. Using

realistic parameter settings for a silicon TQD ($v = 3 \, \text{cm} \times 5 \, \mu\text{m} \times 5 \, \mu\text{m}$, $\epsilon \approx 12$, $\omega_{\text{ph}} = 4.7 \, \text{GHz}$, and $a_l + a_r = 60 \, \text{nm}$) we obtain $g_0 = 2\pi \times 1.96 \, \text{MHz}$. Note that this is the pure vacuum coupling strength, and no field enhancement was included, which can further enhance the strength drastically [68,69]. To make a connection with experiments, it is sometimes more convenient to express the vacuum coupling strength in terms of capacitance and impedance, thus $\mathcal{E} = v\omega_{\text{ph}}\sqrt{Z_0/\pi\hbar/2w}$, with $v = C_{\text{con}}/(C_{\text{con}} + C_{\text{TQD}})$. Here, v is the relative capacitance of the TQD, C_{TQD}, and the capacitance of the connection to the resonator, C_{con}, Z_0 is the characteristic impedance, and w the distance at which the voltage drop occurs [44]. Recent experiments show high impedance

resonators giving rise to a vacuum coupling strength g_0 in the order of $2\pi \times 100 \, \text{MHz}$ [69].

We first construct the real-space wave functions of the states $|0\rangle$, $|1\rangle$, $|2\rangle$, $|3\rangle$, $|4\rangle$, and $|5\rangle$ needed for the transition dipole matrix element. For this we use the formalism of orthonormalized Wannier orbitals [42], which transforms overlapping single-electron wave functions $|\phi_i\rangle$ into an orthonormal basis of maximally localized [70] wave functions $|\Phi_i\rangle$ with $i \in \{1,2,3\}$. Here, the overlaps between the pure single-electron wave functions are denoted as $S_l \equiv \langle\phi_1|\phi_2\rangle$, $S_r \equiv \langle\phi_2|\phi_3\rangle$, and $0 = \langle\phi_1|\phi_3\rangle$ due to the linear arrangement [42]. As a result, we obtain for the position operator in the basis $\{|0\rangle, |1\rangle, |2\rangle, |3\rangle, |4\rangle, |5\rangle\}$

$$
\hat{x} = \begin{pmatrix}
0 & 0 & \frac{1}{\sqrt{2}}x_{12} & \frac{1}{\sqrt{2}}x_{32} & \frac{1}{\sqrt{2}}x_{23} & \frac{1}{\sqrt{2}}x_{21} \\
0 & 0 & \sqrt{\frac{3}{2}}x_{12} & -\sqrt{\frac{3}{2}}x_{32} & -\sqrt{\frac{3}{2}}x_{23} & \sqrt{\frac{3}{2}}x_{21} \\
\frac{1}{\sqrt{2}}x_{21} & \sqrt{\frac{3}{2}}x_{21} & x_{11} - x_{22} & -x_{31} & 0 & 0 \\
\frac{1}{\sqrt{2}}x_{23} & -\sqrt{\frac{3}{2}}x_{23} & -x_{13} & x_{33} - x_{22} & 0 & 0 \\
\frac{1}{\sqrt{2}}x_{32} & -\sqrt{\frac{3}{2}}x_{32} & 0 & 0 & x_{22} - x_{33} & x_{31} \\
\frac{1}{\sqrt{2}}x_{12} & \sqrt{\frac{3}{2}}x_{12} & 0 & 0 & x_{13} & x_{22} - x_{11}
\end{pmatrix},
\tag{26}
$$

where $x_{ij} \equiv \langle\Phi_i|\hat{x}|\Phi_j\rangle$ denotes the transition dipole matrix element between the Wannier orbitals. Under the assumption of equal confinement potentials in each QD, these transition dipole matrix elements can always be chosen real [42].

B. Asymmetric architecture

Placing the TQD inside the cavity such that the electric field aligns with the long axis of the qubit [42] [see Fig. 4(b)] leads to a standard dipole coupling interaction between the qubit and the cavity. States with an asymmetric charge configuration interact with the electromagnetic field of the cavity via their coupling to the opposite charge state, e.g., $|2\rangle \leftrightarrow |3\rangle$ and $|4\rangle \leftrightarrow |5\rangle$, while creating or annihilating a photon in the process. Hence, the qubit-cavity interaction g_A in Eq. (23) can be simplified to

$$
H_A = -e\mathcal{E}\hat{x}(a + a^\dagger), \tag{27}
$$

and the qubit-cavity coupling strength for the asymmetric architecture becomes

$$
g_A \equiv -e\mathcal{E}\langle g|\hat{x}|e\rangle, \tag{28}
$$

where $|g\rangle$ is the ground and $|e\rangle$ the first excited state. In Fig. 5 (left column), the qubit-cavity coupling is calculated numerically and plotted for various parameter settings. The weakest qubit-cavity coupling can be found inside the (1,1,1) charge configuration regime, which is expected due to the symmetric electron distribution. The strongest coupling is located near the four outer DSSs, since at these points a charge transfer only requires a small variation of the detuning parameters to produce a large dipole moment. The asymmetric implementation favors a charge transition associated with a

transfer of one electron from the left QD to the right QD [42], thus $|2\rangle \leftrightarrow |3\rangle$ and $|3\rangle \leftrightarrow |4\rangle$ resulting in strong coupling along a vertical line above and underneath the (1,1,1) charge regime in Fig. 5.

Deep inside the (1,1,1) charge configuration regime, the ground states are $|g\rangle$ and $|e\rangle$, which are $|0\rangle$ and $|1\rangle$ hybridized by a small admixture of the other charge states ($|2\rangle$, $|3\rangle$, $|4\rangle$, $|5\rangle$), hence $\tilde{x} = e^S\hat{x}e^{-S} \approx \hat{x} + [S,\hat{x}] + \frac{1}{2}[S,[S,\hat{x}]] + \cdots$. Here, S is the same Schrieffer-Wolff transformation matrix used to derive the qubit splitting in the low-energy subspace given in Eq. (16). As a result, we obtain a closed analytical expression for the qubit-cavity coupling strength in Eq. (28),

$$
g_A/g_0 = -\sqrt{\frac{3}{2}}\left[\frac{J_l}{t_l}\frac{\text{Re}(x_{12})}{2(a_l + a_r)} - \frac{J_r}{t_r}\frac{\text{Re}(x_{23})}{2(a_l + a_r)}\right]
$$
$$
- \frac{\sqrt{3}}{4}\left[\frac{(\varepsilon - \varepsilon_M)}{U}\frac{J_l^2}{t_l^2}\frac{x_{11}}{a_l + a_r} + \frac{(\varepsilon + \varepsilon_M)}{U}\frac{J_r^2}{t_r^2}\frac{x_{33}}{a_l + a_r}\right].
\tag{29}
$$

Here, the first (second) term in the second line resembles the matrix element of a DQD in the left (right) QD and the center QD [54], which compensate each other at the EO DSS located at $\varepsilon = 0$ and $\varepsilon_M = 0$. Due to the sign change in the first term, the overall matrix element is nonzero at the EO DSS, as may be expected from general considerations. For a completely symmetric setup, $\varepsilon = 0$, $a_l = a_r \equiv a$, $S_l = S_r \equiv S_0$, and $t_l = t_r \equiv t$, which leads to $J_l = J_r \equiv J_0 = 2t^2 U/(U^2 - \varepsilon_M^2)$, $\text{Re}(x_{12}) = -\text{Re}(x_{23}) \approx -3aS_0$,
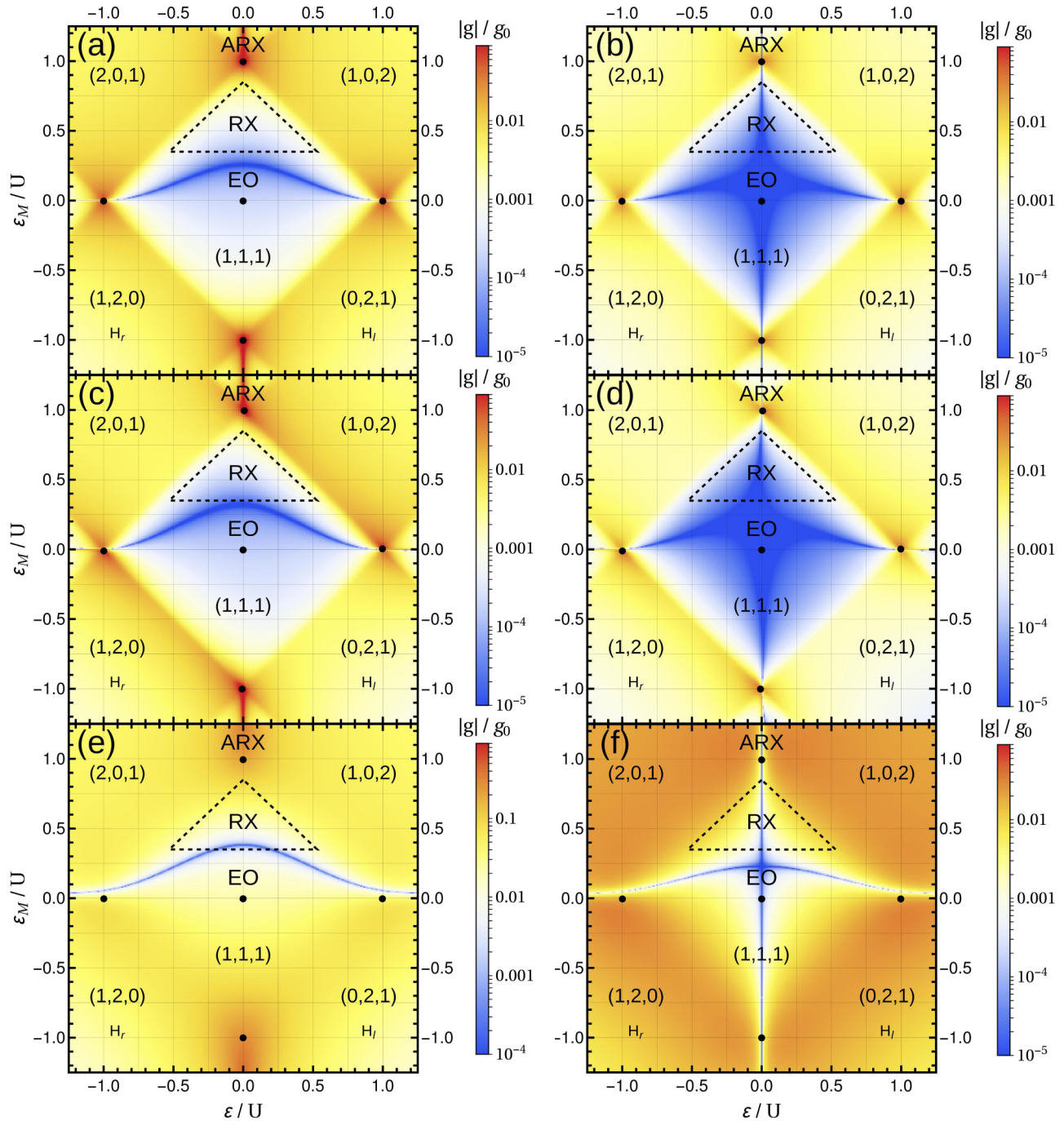
FIG. 5. The qubit-cavity coupling strength g in units of the vacuum coupling strength g_0 as a function of the detuning parameters ε and ε_M for the asymmetric coupling (left column) and symmetric coupling (right column). The parameters are chosen as follows: top row [(a) and (b)] $t_l = t_r = 0.02\,U$, center row [(c) and (d)] $t_l = 0.022\,U$ and $t_r = 0.015\,U$, and bottom row [(e) and (f)] $t_l = t_r = 0.2\,U$. The interdot distances a_l and a_r and the overlaps S_l and S_r are set by the strength of the tunneling parameters [42,71]. The black dots denote the DSSs.

and $x_{11} = -x_{33} \approx -a$, Eq. (29) simplifies to

$$g_{A,0}/g_0 = -\frac{\sqrt{3}}{2}\frac{\varepsilon_M J_0}{U^2 - \varepsilon_M^2} + \sqrt{\frac{3}{2}}\frac{3 J_0 S_0}{2t}. \qquad (30)$$

The first term is identical to the expression for a simple charge model $g_{A,0}/g_0 = -\sqrt{(\partial_\varepsilon J)^2 + 3(\partial_\varepsilon j)^2}/2$ for this choice of parameters [44], and it approaches zero at the DSS while the second term remains finite. The general expression, however, is given in Eq. (29). Introducing $\xi \equiv S_0/t$, we find zero

qubit-cavity coupling at $\xi = \sqrt{2/3}\,\varepsilon_M/(U^2 - \varepsilon_M^2)$, e.g., for the exchange-only DSS $\varepsilon_M = 0$ the condition is $\xi = 0$, thus $S_0 \ll t$.

C. Symmetric architecture

Alternatively, one can place the TQD in the cavity such that the center QD is connected to the transmission line while the outer two QDs are connected with the ground plane [42]

[see Fig. 4(d)]. In this scheme, the electric field is not aligned continuously with the x axis or other axis, but rather, it changes sign and strength in the center. This setup effectively couples the qubit to the detuning parameter ε_M. Figure 4(e) shows the expected electric field as a function of position, which without screening effects can be described as a jump function. To model the electric field, we use

$$\mathcal{E}(\hat{x}) = \frac{1}{\pi} \left\{ \tan^{-1}\left[\frac{\hat{x}}{T(a_l + a_r)} \right] + \frac{\pi(a_l - a_r)}{2(a_l + a_r)} \right\}, \quad (31)$$

where T is a screening parameter that softens the step [see Fig. 4(e)]. Note that $\mathcal{E}$ is an operator here because it is a function of the position operator, hence we obtain for the qubit-cavity interaction

$$H_S = -e\,\mathcal{E}(\hat{x})\,\hat{x}\,(a + a^\dagger). \quad (32)$$

This Hamiltonian can be understood as a generalization of the single-mode dipole interaction [67] $H_{\rm dip} = -e\boldsymbol{E}\cdot\boldsymbol{x}$, in which the electric field $\boldsymbol{E}(\hat{\boldsymbol{x}})$ can be dependent on the position $\hat{\boldsymbol{x}}$ associated with the architecture of the qubit inside the cavity. For the qubit-cavity strength for the symmetric architecture, we find

$$g_S \equiv -e\,\langle g|\,\mathcal{E}(\hat{x})\,\hat{x}\,|e\rangle, \quad (33)$$

with $|g\rangle$ again being the ground state and $|e\rangle$ the first excited state. Unfortunately, g_S cannot be expressed in a closed analytical form in the general case. In Fig. 5 (right column), the results are numerically calculated and plotted for the same parameter settings as for the asymmetric architecture (left column). We find the weakest values for the qubit cavity coupling again deep inside the (1,1,1) charge configuration regime, which is expected due to the large energy required to enable a charge transition. In the vicinity of the expected charge transition areas, which includes the DSS, we find the strongest coupling strength. For $\varepsilon = 0$ and $t_l = t_r$ (for $t_l \neq t_r$ slightly shifted), the symmetric coupling g_S vanishes since for this architecture a charge transition between (1,0,2) and (2,0,1) or (1,2,0) and (0,2,1) is unfavorable with both outer QDs being at the same potential. In contrast to the asymmetric architecture, the symmetric implementation should favor a charge transition associated with an electron transfer only between the left (right) and center QD, thus $|2\rangle \leftrightarrow |4\rangle$ ($|3\rangle \leftrightarrow |5\rangle$). Thus, we expect a strong response seen in a horizontal line from left to right in the $(\varepsilon, \varepsilon_M)$ parameter plane through the center (see Fig. 5). We believe the reason for the absence of this line in the numerical results (Fig. 5, right column) is the need for two simultaneous charge transfers, hence a two-photon process, which is beyond the scope of this model.

Inside the (1,1,1) charge configuration regime and assuming a large screening $T > 1$, thus justifying an expansion of the position-dependent electric field, $E(\hat{x})/\mathcal{E} \approx \hat{x}/\pi T(a_l + a_r) + (a_l - a_r)/2(a_l + a_r)$, we find an analytical expression for the qubit-cavity coupling defined in Eq. (33),

$$g_S/g_0 = \frac{a_l - a_r}{2(a_l + a_r)^2}\,\langle g|\,\hat{x}\,|e\rangle + \frac{1}{\pi T(a_l + a_r)^2}\,\langle g|\,\hat{x}^2\,|e\rangle. \quad (34)$$

The first term $\langle g|\,\hat{x}\,|e\rangle$ is the asymmetric coupling given in Eq. (29), and for the second term we obtain analogously

$$\langle g|\,\hat{x}^2\,|e\rangle = \frac{\sqrt{3}}{4}\left(\frac{J_l^2}{t_l^2}\frac{x_{11}^2}{2} - \frac{J_r^2}{t_r^2}\frac{x_{33}^2}{2} \right)$$
$$+ \frac{\sqrt{3}}{4}\left[\mathrm{Re}(x_{12}) + \frac{(\varepsilon - \varepsilon_M)}{U}\frac{J_l}{t_l}\frac{x_{11}}{\sqrt{2}} \right]^2$$
$$- \frac{\sqrt{3}}{4}\left[\mathrm{Re}(x_{23}) - \frac{(\varepsilon + \varepsilon_M)}{U}\frac{J_r}{t_r}\frac{x_{33}}{\sqrt{2}} \right]^2. \quad (35)$$

For a completely symmetric setup, $\varepsilon = 0$, $a_l = a_r \equiv a$, $S_l = S_r \equiv S_0$, and $t_l = t_r \equiv t$, which leads to $J_l = J_r \equiv J_0$, $\mathrm{Re}(x_{12}) = -\mathrm{Re}(x_{23}) \approx -3aS_0$, and $x_{11} = -x_{33} \approx -a$. Thus, in this fully symmetric case, both Eqs. (35) and (34) yield $g_A = 0$. This result is consistent with previous results using a simple phenomenological approach [42].

D. cQED under the influence of charge noise

In a last step, both architectures are compared with respect to both the qubit-cavity coupling strength and the dephasing T_φ due to charge noise from Sec. III. To achieve strong coupling between the qubit and the cavity, two conditions have to be fulfilled, namely $g > \gamma, \kappa$ with the dephasing rate $\gamma \equiv 1/T_\varphi$, and the cavity-loss rate $\kappa \equiv \omega_{\rm ph}/2\pi Q$ being inversely proportional to the quality factor Q of the cavity [50,53]. Recent experiments indicate that strong coupling is denied by decoherence effects [57,58], thus the limiting condition is

$$g_0 > \frac{1}{T_\varphi\,g/g_0} \quad (36)$$

with the relative qubit-cavity coupling g/g_0 from Eq. (29) for the asymmetric architecture or Eq. (34) for the symmetric one. Alternatively, placing two qubits (here for simplicity assumed to be identical) in the same cavity allows for a long-range two-qubit interaction [42,44,54]. Working in the dispersive regime where the cavity mode is only virtually occupied gives rise to the universal two-qubit iSWAP gate in the time-step [42] $t_{\rm iSWAP} = \omega_{\rm ph}/8Qg^2$. To successfully entangle the qubits, the minimal condition is $t_{\rm iSWAP} < T_\varphi$, thus

$$Q > \frac{\omega_{\rm ph}}{8T_\varphi g^2}. \quad (37)$$

In Fig. 6, the key requirement for strong coupling, Eq. (36), and for entanglement, Eq. (37), are plotted as a function of the detuning parameters for the asymmetric (left column) and the symmetric (right column) architecture. Concerning charge noise, all electric fluctuations except fluctuations in the coupling parameter (ε or ε_M) are neglected due to a strong suppression in ideal resonators. Independently of the used architecture, the strongest response and therefore the weakest requirements (both g_0 and Q) are located at their respective SSS for charge noise if they do not intersect with the lines where $g \approx 0$ for the qubit-cavity coupling. Note that in this simple model, the DSSs play no role since we are considering only a single noise parameter and our results indicate that the asymmetric coupling is beneficial due to a stronger qubit-cavity coupling under the
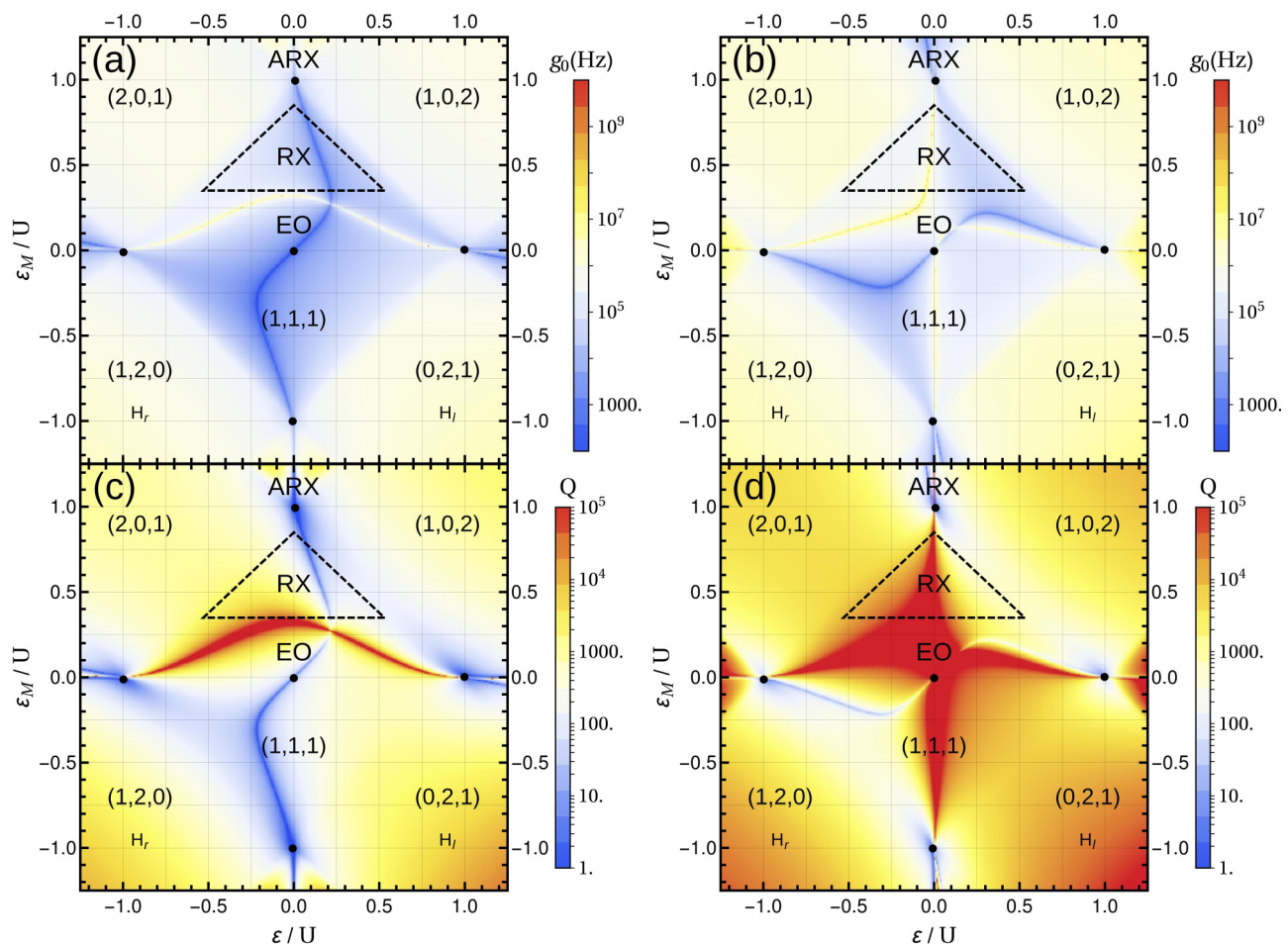
FIG. 6. Top row: The minimal vacuum coupling g_0 [see Eq. (36)] needed to reach strong coupling between the qubit and the cavity under the assumption that qubit dephasing is the dominant loss mechanism. Bottom row: Minimal Q-factor of the cavity [see Eq. (37)] needed for successful entanglement between two qubits in the same cavity. Parts (a) and (c) show the results for the asymmetric architecture and only noise in the asymmetric detuning parameter ε, while (b) and (d) show the results for the symmetric architecture and only noise in the symmetric detuning parameter ε_M. The parameters are chosen as follows: $\omega_{\mathrm{ph}} = 4.7\,\mathrm{GHz}$, $g_0 = 2\pi \times 10\,\mathrm{MHz}$, $t_l = 0.022\,U$, $t_r = 0.015\,U$, and $A_q = (10^{-3}\,U)$, where $q = \varepsilon$ in (a) and $q = \varepsilon_M$ in (b). The datasets for T_φ are obtained from Figs. 7(a) and 7(c). For the scale of T_φ and g, we used an explicit value of $U = 1\,\mathrm{meV}$. The black dots denote the DSS.

assumption of identical noise in both detuning parameters. However, recent investigations suggest that noise coupled to the symmetric detuning parameter ε_M is considerably weaker than for the asymmetric detuning parameter ε [72]. Including tunneling noise does not discriminate further between the two architectures since both are affected in the same way, thus tunneling noise is neglected in this comparison. Estimating realistic numbers, we find that a qubit-cavity vacuum coupling $g_0 > 1\,\mathrm{kHz}$ is sufficient for reaching strong coupling, and one can successfully entangle two qubits with $Q > 10$ if the qubit is operated at the corresponding DSS, i.e., top and bottom DSSs for the asymmetric architecture, and left and right DSSs for the symmetric architecture.

V. CONCLUSION

In this work, we have analyzed different types of three-spin-$\frac{1}{2}$ qubits in an electric environment, either coupled to charge noise or to coherent electric fields in a superconducting strip-line cavity. The first coupling needs to be minimized or

eliminated in order to achieve long-lived qubits. On the other hand, we want to maximize and control the coupling between the qubit and the electric field of the cavity in order to acquire the strong coupling regime needed for a fast long-distance two-qubit gate [42].

In the case of a fluctuating electromagnetic environment, we have provided an extended description considering external electric fluctuations coupled to the qubit through four distinct noisy parameters, two detuning parameters, and two tunneling parameters. We presented and discussed the best suitable working points that take all these couplings into account and minimize the impact limiting the coherence time at the detuning sweet spot. However, no quadruple sweet spot was found suppressing first-order noise effects of all four noisy parameters simultaneously. We found that charge noise coupled to the tunneling parameters is the limiting factor due to the possibility of working on one of the five double sweet spots (DSSs) for noisy detuning parameters. Four of the five DSSs are located each at the crossover regions between connecting asymmetric charge configurations, with the fifth sitting in the
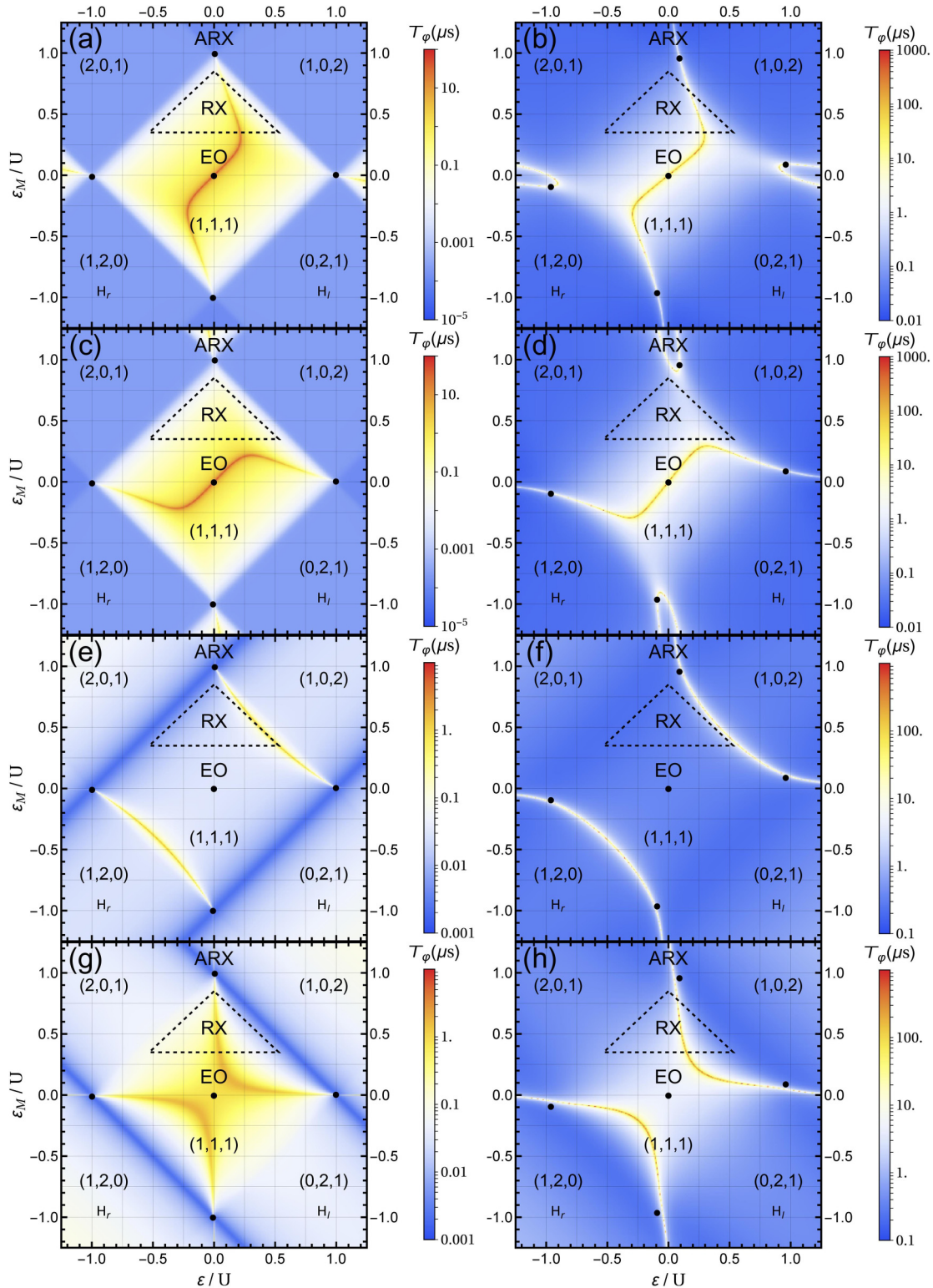
FIG. 7. Dephasing time T_φ due to longitudinal noise for each noisy parameter ε, ε_M, t_l, and t_r individually in the $(\varepsilon, \varepsilon_M)$ plane. Each row shows the dephasing time due to a single noisy parameter (from top to bottom: ε, ε_M, t_l, t_r), while we choose the parameter settings identical in each column. The left column contains the results for weak tunneling and strong noise, while the right column comprises the results for strong tunneling and weak noise. Parameters are set as follows; $t_l = 0.022\,U$, $t_r = 0.015\,U$, $A_q = (10^{-3}\,U)^2$, where $q = \varepsilon$ in (a) and $q = \varepsilon_M$ in (c), and $A_q = (10^{-4}\,U)^2$, where $q = t_l$ in (e) and $q = t_r$ in (g), for the left column, and $t_l = 0.22\,U$, $t_r = 0.15\,U$, $A_q = (10^{-5}\,U)^2$, where $q = \varepsilon$ in (b) and $q = \varepsilon_M$ in (d), and $A_q = (10^{-6}\,U)^2$, where $q = t_l$ in (f) and $q = t_r$ in (h), for the right column. For the scale of T_φ, we used an explicit value of $U = 1$ meV; note that T_φ scales inversely proportional with U. The black dots represent DSS.

center of the $(1,1,1)$ charge configuration regime. We have presented a full map of the dephasing time in the $(\varepsilon, \varepsilon_M)$ parameter plane, taking either the effect of all four noisy parameters, pairs of two noisy parameters, or each noisy parameter individually into account. The optimal strategy depends on the strength of the noise and the strength of each tunneling parameter, however it appears that a symmetric implementation ($t_l = t_r$) typically provides the best result exactly at the DSS, while a slightly asymmetric implementation ($t_l \neq t_r$) elongates the favorable area surrounding the DSS.
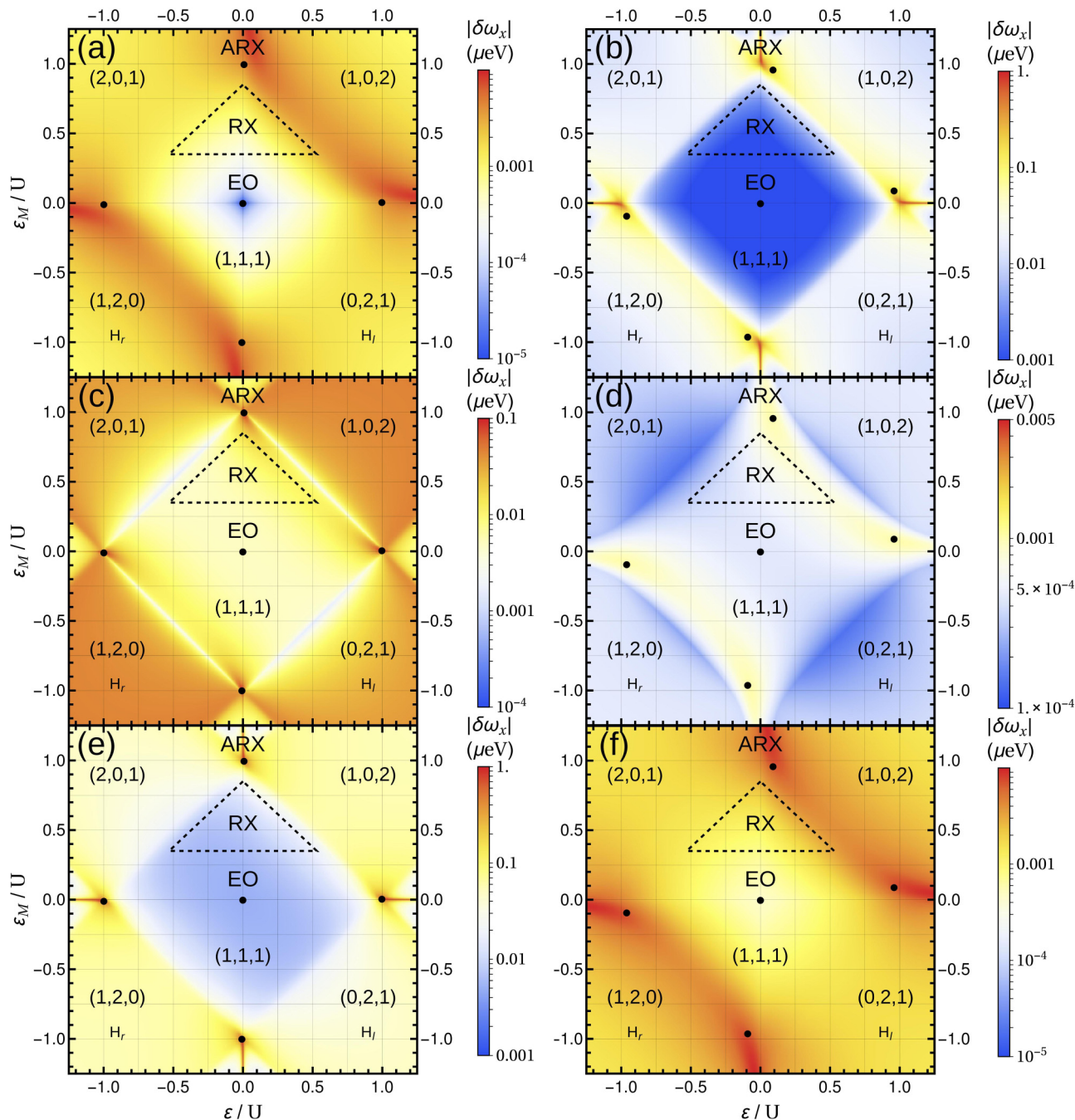

FIG. 8. Impact of transversal noise as a function of the detuning parameters ε and ε_M. In this figure, $\delta\omega_x$ rather than the dephasing time is plotted, thus small values lead to longer coherence times of the qubit. In the top row [(a) and (b)] we consider charge noise only from the two detuning parameters ε and ε_M, in the center row [(c) and (d)] we consider charge noise only from the two tunneling parameters t_l and t_r, and in the bottom row [(e) and (f)] we consider charge noise from all four parameters simultaneously, while we choose the parameter settings identical in each column. The left column contains the results for weak tunneling and strong noise, while the right column comprises the results for strong tunneling and weak noise. The black dots indicate DSS. Parameters are set as follows: $t_l = 0.022\,U, t_r = 0.015\,U, \delta q = 10^{-3}\,U$, where $q = \varepsilon, \varepsilon_M$ in (a) and (e), and $\delta q = 10^{-4}\,U$, where $q = t_l, t_r$ in (c) and (e), for the left column and $t_l = 0.22\,U, t_r = 0.15\,U, \delta q = 10^{-5}\,U$, where $q = \varepsilon, \varepsilon_M$ in (b) and (f), and $\delta q = 10^{-6}\,U$, where $q = t_l, t_r$ in (d) and (f), for the right column. For the scale of $|\delta\omega_x|$ we used an explicit value of $U = 1$ meV.

In the second part of the paper, we presented a full description of the coupling between the qubit and a high-finesse transmission line cavity, taking both basic alignments of connecting the physical qubit and the cavity into account, an asymmetric one being the intuitive where the first and the

last QDs are on opposite potentials with a constant electric field. For the symmetric coupling, both outer QDs are on the same potential while the center QD is connected with the transmission line of the cavity. For both alignments, we have provided a detailed map of the coupling strength
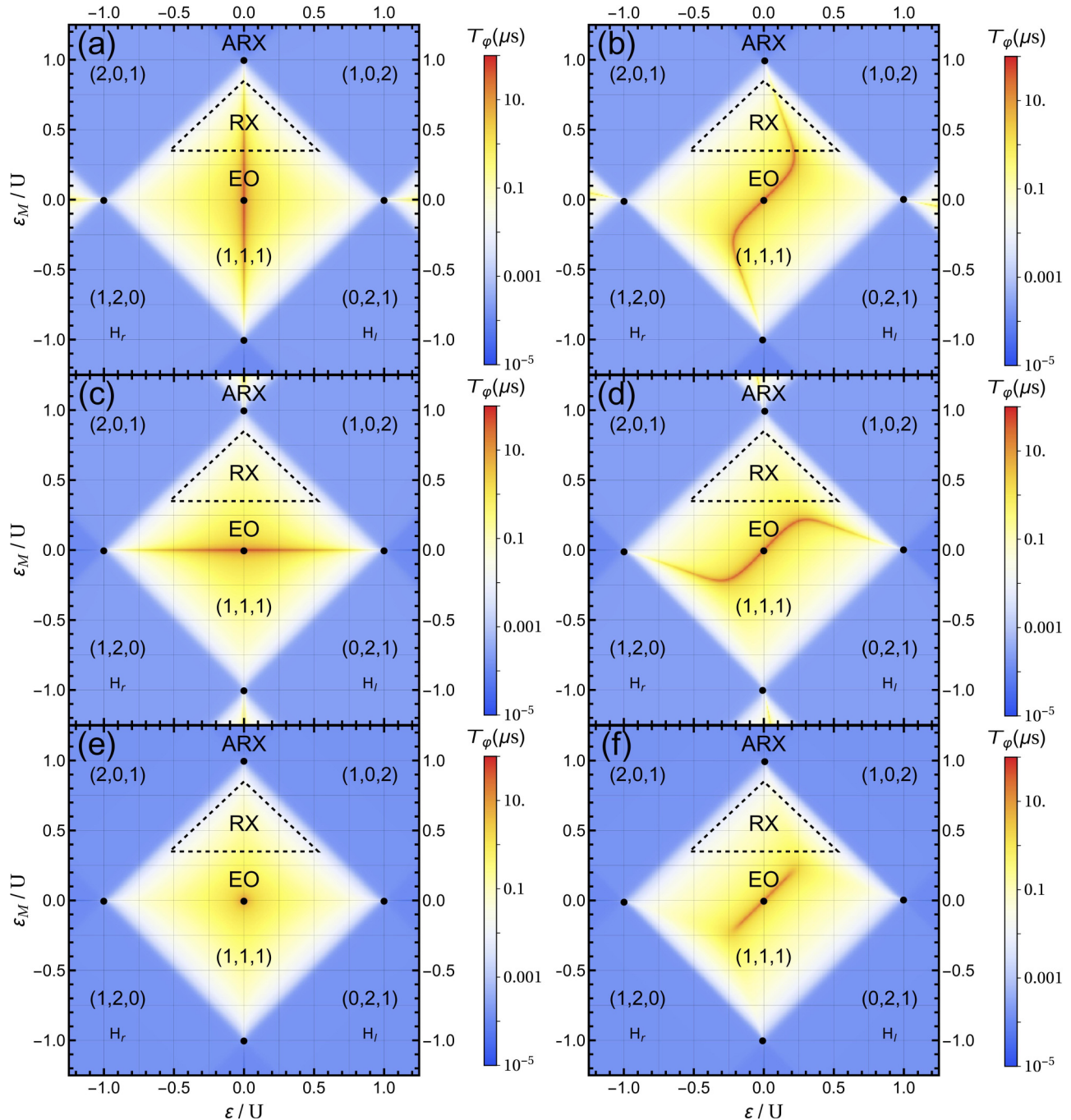

FIG. 9. Comparison of the dephasing time T_φ as a function of the detuning parameters ε and ε_M for symmetric and asymmetric tunnel coupling. In the top row [(a) and (b)] we consider charge noise only from ε, in the center row [(c) and (d)] we consider charge noise only from ε_M, and in the bottom row [(e) and (f)] we consider charge noise from both detuning parameters, ε and ε_M, simultaneously, while we choose the parameter settings identical in each column. The left column comprises the results for symmetric tunneling, while the right column repeats the results for asymmetric tunneling given in Fig. 3(a) and Figs. 7(a) and 7(c). The black dots denote DSS. Parameters are set as follows: $t_l = t_r = t = 0.02\,U$ for the left column and $t_l = 0.022\,U, t_r = 0.015\,U$ for the right column. Furthermore, we set $A_q = (10^{-3}\,U)^2$, where $q = \varepsilon$ in (a) and (b), $q = \varepsilon_M$ in (c) and (d), and $q = \varepsilon, \varepsilon_M$ in (e) and (f). For the scale of T_φ, we used an explicit value of $U = 1$ meV; note that T_φ scales inversely proportional with U.

in parameter space and derived analytical results inside the (1,1,1) charge regime fully agreeing and extending previous results where they exist. Additional features only appearing in the extended model were discussed. The best working points for the asymmetric alignment were located near the $(2,0,1) \leftrightarrow (1,0,2)$ and $(1,2,0) \leftrightarrow (0,2,1)$ charge transitions (the exact position depending on the parameter setting) featuring the top and bottom DSSs as favorable choices. For the symmetric alignment, these points turn out to be less favorable within the scope of our model, and working points near the (1,1,1) charge transitions should be favored in order to obtain decent coupling strength combined with long coherence of the qubit. In a direct comparison assuming identical noise, the asymmetric coupling is beneficial due to the stronger qubit-cavity coupling. However, for the symmetric architecture, we expect an additional influence of two-photon processes, which are beyond the scope of this paper.

APPENDIX A: LONGITUDINAL NOISE COUPLED ONLY THROUGH A SINGLE NOISY PARAMETER

In Fig. 7, the dephasing times are plotted considering the case in which charge noise is coupled to the qubit through only a single noisy parameter for two different parameter settings. Comparing the plots, we find that the resulting dephasing times for detuning noise in ε and ε_M are mirror symmetric to each other with the symmetry axis given by $\varepsilon = \varepsilon_M$, while there is no such symmetry axis for tunneling noise in the general case $t_l \neq t_r$. The SSS for detuning noise are located on a serpentine vertical or horizontal line with the crossing points given by the DSS. For tunneling noise (t_l or t_r) we find that the SSS are located on a narrow curve connecting the top DSS and the right DSS as well as the right DSS and the bottom DSS. A zoom in, however, reveals that the DSSs are not directly located on the line. More precisely, the SSS for tunneling noise in t_l (t_r) are slightly shifted to the right (left) in parameter space. In

contrast to detuning noise, there exist no crossing points for the SSS in tunneling noise.

APPENDIX B: TRANSVERSAL NOISE

In Fig. 8, we plot the transversal effect of charge noise for the same parameter settings as for longitudinal noise. Since the dephasing time cannot be calculated easily for transversal noise, we plot instead $\delta\omega_x = \sum_{q\neq p} |\delta\omega_{x,q}| + |\delta\omega_{x,p}|$ with $q,p \in \{\varepsilon, \varepsilon_M, t_l, t_r\}$ and $\delta\omega_{x,q}$ given in Sec. III A, which is a good measure for the susceptibility of the noise.

In Fig. 8, the combined effects of only noisy detuning (top row), only noisy tunnel coupling (center row), and the combined effects of two noisy detuning and tunneling parameters (bottom row) are shown. Comparison leads to results similar to those for longitudinal noise. The well-protected spot in the center of the (1,1,1) charge configuration considering only detuning noise fades away in the bottom row due to the influence of tunneling noise and becomes as well protected against transversal charge noise as its surroundings. Since the outer DSSs are located at charge transitions, they are very susceptible to transversal noise, and, therefore, they will dephase much faster than other points. A zoom-in, however, reveals that the outer DSSs are not located at a maximum, although they are much more susceptible than the center DSS to transversal charge noise.

APPENDIX C: DEPHASING FOR SYMMETRIC TUNNEL COUPLING

In Fig. 9 we plot the resulting dephasing time T_φ for symmetric tunnel couplings $t_l = t_r = t$ (left column) and asymmetric tunnel coupling $t_l \neq t_r$ (right column), taking into account only the noise from the detuning parameters. Comparing these two situations, we find that in the case of only a single noisy parameter ε (ε_M) and symmetric tunneling, the SSS can be found on a straight vertical (horizontal) line through the center DSS in contrast to the serpentine vertical (horizontal) lines for asymmetric tunneling. Taking both noisy parameters into account, this leads to a single crossing point of the two lines at the center DSS in the symmetric case ($t_l = t_r = t$) while we find an elongated area in the asymmetric case ($t_l \neq t_r$) for the center DSS. Therefore, the asymmetric case allows for greater flexibility in choosing the point of operation while still being protected against longitudinal charge noise.

[1] C. Kloeffel and D. Loss, Prospects for spin-based quantum computing in quantum dots, Annu. Rev. Condens. Matter Phys. **4**, 51 (2013).

[2] J. R. Petta, A. C. Johnson, J. M. Taylor, E. A. Laird, A. Yacoby, M. D. Lukin, C. M. Marcus, M. P. Hanson, and A. C. Gossard, Coherent manipulation of coupled electron spins in semiconductor quantum dots, Science **309**, 2180 (2005).

[3] A. Greilich, D. R. Yakovlev, A. Shabaev, Al. L. Efros, I. A. Yugova, R. Oulton, V. Stavarache, D. Reuter, A. Wieck, and M. Bayer, Mode locking of electron spin coherences in singly charged quantum dots, Science **313**, 341 (2006).

[4] F. H. L. Koppens, K. C. Nowack, and L. M. K. Vandersypen, Spin Echo of a Single Electron Spin in a Quantum Dot, Phys. Rev. Lett. **100**, 236802 (2008).

[5] A. Morello, J. J. Pla, F. A. Zwanenburg, K. W. Chan, K. Y. Tan, H. Huebl, M. Mottonen, C. D. Nugroho, C. Yang, J. A. van Donkelaar, A. D. C. Alves, D. N. Jamieson, C. C. Escott, L. C. L. Hollenberg, R. G. Clark, and A. S. Dzurak, Single-shot readout of an electron spin in silicon, Nature (London) **467**, 687 (2010).

[6] B. M. Maune, M. G. Borselli, B. Huang, T. D. Ladd, P. W. Deelman, K. S. Holabird, A. A. Kiselev, I. Alvarado-Rodriguez,

R. S. Ross, A. E. Schmitz, M. Sokolich, C. A. Watson, M. F. Gyure, and A. T. Hunter, Coherent singlet-triplet oscillations in a silicon-based double quantum dot, Nature (London) **481**, 344 (2012).

[7] J. J. Pla, K. Y. Tan, J. P. Dehollain, W. H. Lim, J. J. L. Morton, D. N. Jamieson, A. S. Dzurak, and A. Morello, A single-atom electron spin qubit in silicon, Nature (London) **489**, 541 (2012).

[8] C. H. Yang, A. Rossi, R. Ruskov, N. S. Lai, F. A. Mohiyaddin, S. Lee, C. Tahan, G. Klimeck, A. Morello, and A. S. Dzurak, Spin-valley lifetimes in a silicon quantum dot with tunable valley splitting, Nat. Commun. **4**, 2069 (2013).

[9] D. D. Awschalom, L. C. Bassett, A. S. Dzurak, E. L. Hu, and J. R. Petta, Quantum spintronics: Engineering and manipulating atom-like spins in semiconductors, Science **339**, 1174 (2013).

[10] J. T. Muhonen, J. P. Dehollain, A. Laucht, F. E. Hudson, R. Kalra, T. Sekiguchi, K. M. Itoh, D. N. Jamieson, J. C. McCallum, A. S. Dzurak, and A. Morello, Storing quantum information for 30 seconds in a nanoelectronic device, Nat. Nano **9**, 986 (2014).

[11] K. Eng, T. D. Ladd, A. Smith, M. G. Borselli, A. A. Kiselev, B. H. Fong, K. S. Holabird, T. M. Hazard, B. Huang, P. W. Deelman, I. Milosavljevic, A. E. Schmitz, R. S. Ross, M. F. Gyure, and A. T. Hunter, Isotopically enhanced triple-quantum-dot qubit, Sci. Adv. **1**, e1500214 (2015).

[12] M. D. Reed, B. M. Maune, R. W. Andrews, M. G. Borselli, K. Eng, M. P. Jura, A. A. Kiselev, T. D. Ladd, S. T. Merkel, I. Milosavljevic, E. J. Pritchett, M. T. Rakher, R. S. Ross, A. E. Schmitz, A. Smith, J. A. Wright, M. F. Gyure, and A. T. Hunter, Reduced Sensitivity to Charge Noise in Semiconductor Spin Qubits via Symmetric Operation, Phys. Rev. Lett. **116**, 110402 (2016).

[13] R. Hanson, L. P. Kouwenhoven, J. R. Petta, S. Tarucha, and L. M. K. Vandersypen, Spins in few-electron quantum dots, Rev. Mod. Phys. **79**, 1217 (2007).

[14] F. A. Zwanenburg, A. S. Dzurak, A. Morello, M. Y. Simmons, L. C. L. Hollenberg, G. Klimeck, S. Rogge, S. N. Coppersmith, and M. A. Eriksson, Silicon quantum electronics, Rev. Mod. Phys. **85**, 961 (2013).

[15] W. A. Coish and D. Loss, Hyperfine interaction in a quantum dot: Non-Markovian electron spin dynamics, Phys. Rev. B **70**, 195340 (2004).

[16] S. Mehl and D. P. DiVincenzo, Noise analysis of qubits implemented in triple quantum dot systems in a Davies master equation approach, Phys. Rev. B **87**, 195309 (2013).

[17] J.-T. Hung, J. Fei, M. Friesen, and X. Hu, Decoherence of an exchange qubit by hyperfine interaction, Phys. Rev. B **90**, 045308 (2014).

[18] M. M. Glazov, Magnetic field effects on spin relaxation in heterostructures, Phys. Rev. B **70**, 195314 (2004).

[19] M. Prada and D. Pfannkuche, Anisotropy of spin coherence in high mobility quantum wells with arbitrary magnetic fields, arXiv:1605.03399 [cond-mat.mes-hall].

[20] I. V. Yurkevich, J. Baldwin, I. V. Lerner, and B. L. Altshuler, Decoherence of charge qubit coupled to interacting background charges, Phys. Rev. B **81**, 121305 (2010).

[21] O. E. Dial, M. D. Shulman, S. P. Harvey, H. Bluhm, V. Umansky, and A. Yacoby, Charge Noise Spectroscopy Using Coherent Exchange Oscillations in a Singlet-Triplet Qubit, Phys. Rev. Lett. **110**, 146804 (2013).

[22] J. M. Taylor, V. Srinivasa, and J. Medford, Electrically Protected Resonant Exchange Qubits in Triple Quantum Dots, Phys. Rev. Lett. **111**, 050502 (2013).

[23] J. Fei, J.-T. Hung, T. S. Koh, Y.-P. Shim, S. N. Coppersmith, X. Hu, and M. Friesen, Characterizing gate operations near the sweet spot of an exchange-only qubit, Phys. Rev. B **91**, 205434 (2015).

[24] M. Russ and G. Burkard, Asymmetric resonant exchange qubit under the influence of electrical noise, Phys. Rev. B **91**, 235411 (2015).

[25] Y.-P. Shim and C. Tahan, Charge-noise-insensitive gate operations for always-on, exchange-only qubits, Phys. Rev. B **93**, 121410 (2016).

[26] D. A. Lidar and T. A. Brun, *Quantum Error Correction* (Cambridge University Press, Cambridge, 2013).

[27] J. R. West and B. H. Fong, Exchange-only dynamical decoupling in the three-qubit decoherence free subsystem, New J. Phys. **14**, 083002 (2012).

[28] F. Setiawan, H.-Y. Hui, J. P. Kestner, X. Wang, and S. Das Sarma, Robust two-qubit gates for exchange-coupled qubits, Phys. Rev. B **89**, 085314 (2014).

[29] N. Rohling and G. Burkard, Optimizing electrically controlled echo sequences for the exchange-only qubit, Phys. Rev. B **93**, 205434 (2016).

[30] D. Vion, A. Aassime, A. Cottet, P. Joyez, H. Pothier, C. Urbina, D. Esteve, and M. H. Devoret, Manipulating the quantum state of an electrical circuit, Science **296**, 886 (2002).

[31] E. Paladino, Y. M. Galperin, G. Falci, and B. L. Altshuler, $1/f$ noise: Implications for solid-state quantum information, Rev. Mod. Phys. **86**, 361 (2014).

[32] T. Takakura, M. Pioro-Ladrière, T. Obata, Y.-S. Shin, R. Brunner, K. Yoshida, T. Taniyama, and S. Tarucha, Triple quantum dot device designed for three spin qubits, Appl. Phys. Lett. **97**, 212104 (2010).

[33] L. Gaudreau, G. Granger, A. Kam, G. C. Aers, S. A. Studenikin, P. Zawadzki, M. Pioro-Ladriere, Z. R. Wasilewski, and A. S. Sachrajda, Coherent control of three-spin states in a triple quantum dot, Nat. Phys. **8**, 54 (2012).

[34] J. Medford, J. Beil, J. M. Taylor, E. I. Rashba, H. Lu, A. C. Gossard, and C. M. Marcus, Quantum-Dot-Based Resonant Exchange Qubit, Phys. Rev. Lett. **111**, 050501 (2013).

[35] M. Veldhorst, C. H. Yang, J. C. C. Hwang, W. Huang, J. P. Dehollain, J. T. Muhonen, S. Simmons, A. Laucht, F. E. Hudson, K. M. Itoh, A. Morello, and A. S. Dzurak, A two-qubit logic gate in silicon, Nature (London) **526**, 410 (2015).

[36] D. A. Lidar and K. Birgitta Whaley, *Decoherence-Free Subspaces and Subsystems,* in Irreversible Quantum Dynamics (Springer, Berlin, 2003), pp. 83–120.

[37] D. P. DiVincenzo, D. Bacon, J. Kempe, G. Burkard, and K. B. Whaley, Universal quantum computation with the exchange interaction, Nature (London) **408**, 339 (2000).

[38] E. A. Laird, J. M. Taylor, D. P. DiVincenzo, C. M. Marcus, M. P. Hanson, and A. C. Gossard, Coherent spin manipulation in an exchange-only qubit, Phys. Rev. B **82**, 075403 (2010).

[39] Z. Shi, C. B. Simmons, J. R. Prance, J. K. Gamble, T. S. Koh, Y.-P. Shim, X. Hu, D. E. Savage, M. G. Lagally, M. A. Eriksson, M. Friesen, and S. N. Coppersmith, Fast Hybrid Silicon Double-Euantum-Dot Qubit, Phys. Rev. Lett. **108**, 140503 (2012).

[40] T. S. Koh, J. K. Gamble, M. Friesen, M. A. Eriksson, and S. N. Coppersmith, Pulse-Gated Quantum-Dot Hybrid Qubit, Phys. Rev. Lett. **109**, 250503 (2012).

[41] G. Cao, H.-O. Li, G.-D. Yu, B.-C. Wang, B.-B. Chen, X.-X. Song, M. Xiao, G.-C. Guo, H.-W. Jiang, X. Hu, and G.-P. Guo, Tunable Hybrid Qubit in a GaAs Double Quantum Dot, Phys. Rev. Lett. **116**, 086801 (2016).

[42] M. Russ and G. Burkard, Long distance coupling of resonant exchange qubits, Phys. Rev. B **92**, 205412 (2015).

[43] S. Amasha, K. MacLean, I. P. Radu, D. M. Zumbühl, M. A. Kastner, M. P. Hanson, and A. C. Gossard, Electrical Control of Spin Relaxation in a Quantum Dot, Phys. Rev. Lett. **100**, 046803 (2008).

[44] V. Srinivasa, J. M. Taylor, and C. Tahan, Entangling distant resonant exchange qubits via circuit quantum electrodynamics, arXiv:1603.04829 [cond-mat.mes-hall].

[45] B. H. Fong and S. M. Wandzura, Universal quantum computation and leakage reduction in the 3-qubit decoherence free subsystem, Quantum Inf. Comput. **11**, 1003 (2011).

[46] A. C. Doherty and M. P. Wardrop, Two-Qubit Gates for Resonant Exchange Qubits, Phys. Rev. Lett. **111**, 050503 (2013).

[47] M. P. Wardrop and A. C. Doherty, Characterization of an exchange-based two-qubit gate for resonant exchange qubits, Phys. Rev. B **93**, 075436 (2016).

[48] A. Pal, E. I. Rashba, and B. I. Halperin, Driven Nonlinear Dynamics of Two Coupled Exchange-Only Qubits, Phys. Rev. X **4**, 011012 (2014).

[49] A. Pal, E. I. Rashba, and B. I. Halperin, Exact cnot gates with a single nonlocal rotation for quantum-dot qubits, Phys. Rev. B **92**, 125409 (2015).

[50] A. Blais, R.-S. Huang, A. Wallraff, S. M. Girvin, and R. J. Schoelkopf, Cavity quantum electrodynamics for superconducting electrical circuits: An architecture for quantum computation, Phys. Rev. A **69**, 062320 (2004).

[51] A. Wallraff, D. I. Schuster, A. Blais, L. Frunzio, R. S. Huang, J. Majer, S. Kumar, S. M. Girvin, and R. J. Schoelkopf, Strong coupling of a single photon to a superconducting qubit using circuit quantum electrodynamics, Nature (London) **431**, 162 (2004).

[52] A. Imamoglu, D. D. Awschalom, G. Burkard, D. P. DiVincenzo, D. Loss, M. Sherwin, and A. Small, Quantum Information Processing Using Quantum Dot Spins and Cavity QED, Phys. Rev. Lett. **83**, 4204 (1999).

[53] L. Childress, A. S. Sørensen, and M. D. Lukin, Mesoscopic cavity quantum electrodynamics with quantum dots, Phys. Rev. A **69**, 042302 (2004).

[54] G. Burkard and A. Imamoglu, Ultra-long-distance interaction between spin qubits, Phys. Rev. B **74**, 041307 (2006).

[55] J. M. Taylor and M. D. Lukin, Dephasing of quantum bits by a quasi-static mesoscopic environment, Quant. Inf. Proc. **5**, 503 (2006).

[56] X. Hu, Y.-x. Liu, and F. Nori, Strong coupling of a spin qubit to a superconducting stripline cavity, Phys. Rev. B **86**, 035314 (2012).

[57] K. D. Petersson, L. W. McFaul, M. D. Schroer, M. Jung, J. M. Taylor, A. A. Houck, and J. R. Petta, Circuit quantum electrodynamics with a spin qubit, Nature (London) **490**, 380 (2012).

[58] J. J. Viennot, M. C. Dartiailh, A. Cottet, and T. Kontos, Coherent coupling of a single spin to microwave cavity photons, Science **349**, 408 (2015).

[59] F. Beaudoin, A. Blais, and W. A. Coish, Hamiltonian engineering for robust quantum state transfer and qubit readout in cavity QED, arXiv:1602.05090 [quant-ph].

[60] B. Royer, A. L. Grimsmo, N. Didier, and A. Blais, Fast and high-fidelity entangling gate through parametrically modulated longitudinal coupling, arXiv:1603.04424 [quant-ph].

[61] F. Beaudoin, D. Lachance-Quirion, W. A. Coish, and M. Pioro-Ladrière, Coupling a single electron spin to a microwave resonator: Controlling transverse and longitudinal couplings, arXiv:1606.04736 [cond-mat.mes-hall].

[62] G. Burkard and J. R. Petta, Dispersive readout of valley splittings in cavity-coupled silicon quantum dots, arXiv:1607.08801 [cond-mat.mes-hall].

[63] B. M. Freeman, J. S. Schoenfield, and H.-W. Jiang, Comparison of low frequency charge noise in identically patterned si/sio2 and si/sige quantum dots, Appl. Phys. Lett. **108**, 253108 (2016).

[64] S. Bravyi, D. P. Divincenzo, and D. Loss, Schrieffer-Wolff transformation for quantum many-body systems, Ann. Phys. (N.Y.) **326**, 2793 (2011).

[65] D. Loss and D. P. DiVincenzo, Quantum computation with quantum dots, Phys. Rev. A **57**, 120 (1998).

[66] F. Martins, F. K. Malinowski, P. D. Nissen, E. Barnes, S. Fallahi, G. C. Gardner, M. J. Manfra, C. M. Marcus, and F. Kuemmeth, Noise Suppression Using Symmetric Exchange Gates in Spin Qubits, Phys. Rev. Lett. **116**, 116801 (2016).

[67] C. Cohen-Tannoudji, J. Dupont-Roc, and G. Grynberg, *Photons and Atoms: Introduction to Quantum Electrodynamics* (Wiley-VCH, Weinheim, 2007).

[68] G. Tosi, F. A. Mohiyaddin, H. Huebl, and A. Morello, Circuit-quantum electrodynamics with direct magnetic coupling to single-atom spin qubits in isotopically enriched 28si, AIP Adv. **4**, 087122 (2014).

[69] N. Samkharadze, A. Bruno, P. Scarlino, G. Zheng, D. P. DiVincenzo, L. DiCarlo, and L. M. K. Vandersypen, High-kinetic-inductance superconducting nanowire resonators for circuit QED in a magnetic field, Phys. Rev. Appl. **5**, 044004 (2016).

[70] N. Marzari, A. A. Mostofi, J. R. Yates, I. Souza, and D. Vanderbilt, Maximally localized Wannier functions: Theory and applications, Rev. Mod. Phys. **84**, 1419 (2012).

[71] G. Burkard, D. Loss, and D. P. DiVincenzo, Coupled quantum dots as quantum gates, Phys. Rev. B **59**, 2070 (1999).

[72] M. Friesen, M. A. Eriksson, and S. N. Coppersmith, A decoherence-free subspace for charge: The quadrupole qubit, arXiv:1605.01797 [quant-ph].